

PADM2M: a penalized maximum likelihood model of the 0–2 Ma palaeomagnetic axial dipole moment

L. B. Ziegler,¹ C. G. Constable,¹ C. L. Johnson² and L. Tauxe³

¹*Institute of Geophysics and Planetary Physics, Scripps Institution of Oceanography, University of California, San Diego, 9500 Gilman Drive, La Jolla, CA 92093-0225, USA. E-mail: lziegler@ucsd.edu*

²*Department of Earth and Ocean Sciences, University of British Columbia, 6339 Stores Road, Vancouver, B.C. V6T 1Z4, Canada*

³*Scripps Institution of Oceanography, University of California, San Diego, 9500 Gilman Drive, La Jolla, CA 92093-0220, USA*

Accepted 2010 November 29. Received 2010 November 12; in original form 2010 February 4

SUMMARY

We present a new time-varying model for palaeomagnetic axial dipole moment (PADM) for the past 2 Myr and compare it with earlier virtual axial dipole moment (VADM) reconstructions which have been based on stacking and averaging scaled relative palaeointensity records. The PADM is derived from both absolute and relative palaeointensity data and constructed using a new penalized maximum likelihood (PML) approach to recover a cubic B-spline representation of axial-dipole field variations on million year timescales. The PML method is explicitly intended to reduce bias in estimating the true axial dipole moment that arises in average VADM reconstructions. We apply the PML method to a set of 96 032 published data (1800 palaeointensities from igneous rocks, 3300 archaeointensities and 86 relative palaeointensity time-series of variable lengths and resolutions). Two models are discussed: PADM2Mp is a trial model based on a subset of the nine longest available sedimentary records; PADM2M uses a comprehensive data set (76 records, 81 446 data; 10 records were eliminated) and is our preferred model. PADM2M has a lower mean than existing VADM reconstructions but shows similarities in long-period variability. Some differences in timing, amplitude and resolution of certain features can be attributed to variations in age assignments. Others result from our more comprehensive data set and a reduction in bias attributable to PML modelling. PADM2M has an average axial dipole moment over 0–2 Ma of $5.3 \times 10^{22} \text{ Am}^2$ with a standard deviation of $1.5 \times 10^{22} \text{ Am}^2$. The Brunhes chron average ($6.2 \times 10^{22} \text{ Am}^2$) is higher than for earlier epochs of Matuyama ($4.8 \times 10^{22} \text{ Am}^2$), as seen in some previous studies. The power spectrum for our model agrees with previous estimates of the global palaeomagnetic power spectrum for frequencies up to about 10^2 Myr^{-1} . We see no distinctive evidence in the power spectrum for orbital forcing of geodynamo behaviour.

Key words: Archaeomagnetism; Magnetic field; Palaeointensity; Palaeomagnetic secular variation.

1 INTRODUCTION

Earth's history can be investigated by looking at the palaeomagnetic record. Dynamic processes in the core drive the continuously changing geomagnetic field, which is recorded on Earth's surface by newly forming igneous rocks and sediments. On centennial and millennial timescales, time-varying spherical harmonic models of Earth's magnetic field derived from historical, archaeomagnetic and/or palaeomagnetic data (Jackson *et al.* 2000; Korte & Constable 2005; Korte *et al.* 2009) have yielded insights into dynamo processes (e.g. Amit & Olson 2006; Dumberry & Finlay 2007; Wardinski & Korte 2008).

On million year timescales, time-varying reconstructions of palaeomagnetic field behaviour are limited by the quantity and quality of available data. As a starting point, the field is often approximated by a dipole, or more specifically a field resulting

from a geocentric axial dipole (GAD) source. The GAD approximation is sometimes made under the assumption that it provides an accurate representation of the time-averaged field structure. Numerous studies have shown that this is not exactly the case (Wilson 1970; Johnson & McFadden 2007; Johnson *et al.* 2008), but it remains a useful starting point for understanding field changes on long timescales. The axial-dipole alone represents the largest geographic and temporal variations in the geomagnetic field, and (depending on the available data) may be the only structure recoverable through the data uncertainties. The spatial structure has large geographic variability but is static, so time variations under the GAD model are restricted to changes in the strength of the palaeomagnetic axial-dipole moment (PADM), the terminology we will use for strength of the axial dipole. When palaeointensity data are considered under the GAD model they are usually converted into virtual axial dipole

moment (VADM) data—the VADM is the equivalent moment associated with a dipole source aligned with Earth’s rotation axis that is needed to produce the palaeointensity datum at the latitude of the specific observation. This transformation removes the geographic variations in palaeointensity that would be expected for an axial-dipole source. The goal of this work is to use VADM data to find optimal estimates for the PADM.

Under the GAD approximation, a number of time-varying palaeomagnetic field strength reconstructions have been made both from globally distributed data (Valet *et al.* 2005; Channell *et al.* 2009) and regional data sets (Laj *et al.* 2000; Stoner *et al.* 2002). These efforts involve stacking and averaging relative palaeointensity (RPI) time-series derived from sediments and sometimes calibrating the resulting stack to absolute VADM variations through comparison with absolute palaeointensity (API) derived from igneous rocks.

These VADM models are somewhat limited in temporal resolution, and are clearly limited by the fixed geographic structure, but nevertheless provide useful information for testing the feasibility of particular dynamo regimes. Investigations to date have included characterizing the timescales associated with field reversals and excursions (Valet *et al.* 2005), observations of possible asymmetry in the field decay and growth processes associated with reversals (commonly referred to as ‘sawtooth’ palaeointensity signals), for example, Valet & Meynadier (1993), McFadden & Merrill (1997) and Valet *et al.* (2005), deriving the power spectrum associated with field intensities including corner frequencies and falloff (Constable & Johnson 2005; Driscoll & Olson 2009), among other things. VADM models are also used as magnetostratigraphic tools (e.g. Stoner *et al.* 1998; Brachfeld *et al.* 2003) with global intensity variations providing much higher resolution than the geomagnetic reversal record, but these applications are not the focus of this study.

In this paper, we first describe the available VADM data (Section 2), then motivate, develop and apply a new approach for recovering PADM variation on million year timescales (Section 3). We show that a simple average of VADM data leads to a biased estimate of the PADM (Appendix A), illustrating that the noise distribution associated with VADM data is non-Gaussian and asymmetric. We introduce a simple but flexible parametric model for the noise that can take account of variability among the various data records. We develop a penalized maximum likelihood (PML) inversion procedure to recover estimates of PADM that are less biased and apply it to construct a regularized, cubic B-spline model of time-varying PADM over the last 2 Myr (Section 3, Appendix B). The resulting PADM2M model is made from a combination of globally distributed API data and RPI records from sediment cores. As part of the modelling procedure we solve for scaling factors needed to calibrate the RPI records to VADM. Our results are presented in Section 4, where we describe a preliminary model PADM2Mp constructed from nine records, each spanning more than 1.5 Myr and including the Brunhes/Matuyama polarity reversal, and our preferred model PADM2M derived from a much larger and more heterogeneous set of currently available RPI time-series.

2 VADM DATA FOR GLOBAL MODELLING

For the construction of time-varying palaeomagnetic field models, we would ideally use many tightly dated, globally distributed records of intensity variation. In practice, the data available consist of spot recordings (from igneous rocks and archaeological artefacts) of absolute field intensity values and time-series (from sediments)

of relative field intensity variations. The spot recordings are dated using a range of techniques with correspondingly diverse uncertainties. Although this statement is true of sedimentary data as well, the sequential nature of magnetic measurements taken at regular spacings through a core mean that at least the temporal order is certain. The time-series generated from long cores provide information on field strength variations for up to millions of years but cannot constrain the absolute field strength, while the spot recordings adequately constrain field strength but on their own are too sparse to give a picture of field variations on million year timescales. Our modelling uses both absolute palaeointensities (API) and RPI time-series to develop a composite picture of field intensity variations over the last 2 Myr.

All data used in this study are drawn from previously published work. We take advantage of freely available, public domain databases in our efforts to build comprehensive data sets suitable for analysis (described below). The exact data compilation used in this study is archived in the EarthRef Digital Archive (<http://earthref.org/erda/1138>) along with the PADM2M model (<http://earthref.org/erda/1139>).

2.1 API data

API data are derived from iron-bearing igneous rocks and archaeological artefacts which were once hot enough to become magnetized in response to the Earth’s magnetic field present at their formation. As these materials cool through the blocking temperature spectrum of the relevant magnetic minerals, the remanent magnetism is frozen in. The theory of thermal remanence acquisition is well understood for simple systems involving single domain magnetite and forms the basis for the pioneering Thellier & Thellier (1959) laboratory technique to recover the ancient magnetic field strength which produced the magnetization of a given sample. There are now many variants on the original method and new methods, that are intended to reduce measurement error, sample alteration and incorporate internal consistency checks on assumptions inherent to the method. In addition, various strategies are sometimes employed for making cooling rate or anisotropy corrections (see Tauxe & Yamazaki (2007) for a more comprehensive discussion of modern palaeointensity laboratory techniques). Lack of uniformity in laboratory procedures and natural variations in source materials lead to a broad range of contributions to uncertainties in the resulting palaeointensity data.

We are interested in using as many data as possible and do not restrict our data set to any particular minimum uncertainty level, quality criteria, laboratory procedure or source material. In a detailed analysis of a diverse palaeointensity data set, Ziegler *et al.* (2008) found that field strength statistics derived from the set of all available records and subsets which excluded less reliable data (based on a few specific criteria) were not significantly different. They concluded that although the use of less reliable data is not the preferred strategy, it does not significantly bias results. This further supports the strategy of using all available palaeointensity data in our models. Ziegler *et al.* (2008) did note a statistical difference between data derived from archaeological and igneous sources. Here, we use both material types, but treat them as two distinct data sets.

The most recent Geomag50.v2 database (Donadini *et al.* 2009) compiles API data from archaeological and igneous sources with ages less than 50 kyr. We use all data in this database except for some submarine basaltic glass data which have poorer age constraints than the rest of the database. In total, we take 4236 data from Geomag50.v2 as of 2009 June (902 from igneous sources, 3334

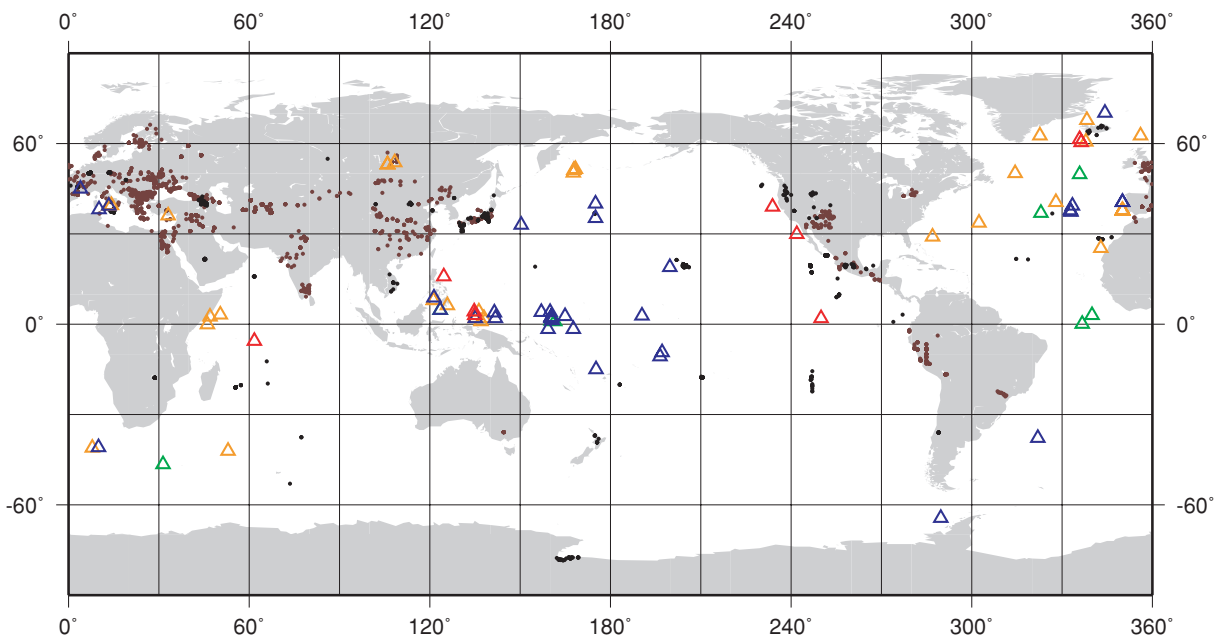


Figure 1. Geographic distribution of data used in this study. Small circles are for API data (brown for archaeomagnetic data, black for igneous data). Triangles represent sediment cores, where red, blue, yellow and green correspond to P0, Long, Young and Reversal records, respectively (see text).

from archaeological or unspecified materials). For data older than 50 kyr, we look to the PINT palaeointensity database, PINT08 (Biggin *et al.* 2009). This database contains thousands of data covering all ages older than 50 kyr, but we only use the 868 data with ages greater than 50 kyr and less than 2 Myr. We have incorporated improved ages (Singer *et al.* 2008) for 16 data. Finally, we have added 30 data from Lawrence *et al.* (2009), giving us a total of 898 data with nominal ages of 50 kyr–2 Myr.

The geographic and temporal distributions of the API data are given in Figs 1 and 2, respectively. Data are mainly concentrated at northern mid-latitudes, although there are some available in the southern hemisphere. Archaeomagnetic data are generally less than 10 kyr in age and are particularly dense in Europe. Hawaii is also noteworthy as a source of volcanic palaeointensity records. The age distribution of API data is very non-uniform, with a disproportionate number of archaeomagnetic contributions and young volcanics (0–10 ka). Age uncertainties are also highly variable and often poorly documented. However if we take the age information at face value, there are data distributed throughout the past 2 Myr (see Fig. 2).

2.2 RPI data

Marine sediments also carry remanent magnetism. However, as opposed to the thermal remanence acquisition process involved in magnetizing API source materials, sediments acquire a detrital remanent magnetization (DRM). As already-magnetized detrital grains settle through the water column, they can freely rotate to align with the ambient geomagnetic field. A sample's magnetization depends primarily on the field strength, the amount and type of magnetic material present and environmental factors such as the sedimentary matrix; after normalizing for variations in the amount of magnetic material present in the core, the normalized magnetization is supposed to be linearly related to field strength. For already published data it is generally impractical to account for the influ-

ence of changing environmental factors (e.g. nature of the sediment matrix, magnetic grain size) on the core's magnetization. Any such factors present will just be incorporated into our noise model. Beyond this, theory needed to recover absolute palaeointensities from materials which have a DRM is an area of active research. In addition, some sedimentary environments and/or high field strength can sometimes lead to departures from the linear relationship between normalized magnetism and field strength. A more thorough discussion of sediment RPIs and DRM can be found in Tauxe & Yamazaki (2007) and Valet (2003). Although limited by the absence of theory to recover absolute field intensity, sediments have the advantage of being continuously deposited: sequential measurements down a sediment core give an ordered time-series of relative intensity variations. The individual cores reflect a variety of source material compositions, sedimentation rates (and hence, signal resolution and smoothing), normalization proxies and laboratory procedures.

Recent efforts by the palaeomagnetic community have produced a large, geographically diverse set of RPI time-series. Numerous lacustrine records have been used in Holocene geomagnetic models (Korte *et al.* 2009), but we omit almost all these records from our collection because we already have good coverage from archaeomagnetic data with generally better age constraints. We primarily use marine cores which provide longer, but typically lower resolution, time-series.

We use all the RPI records from the SEDPI06 collection of sediment cores assembled by Tauxe & Yamazaki (2007) whose timescales are independent of correlations based on RPI information and for which we were able to acquire the data. One significant advantage of using the SEDPI06 compilation is that all data have been adjusted to conform to a common geomagnetic polarity time scale (GPTS) with reversal ages tied to CK95 (Cande & Kent 1995). This leads to some minor variations from the age models originally published with the data, but provides us with an internally consistent data set.

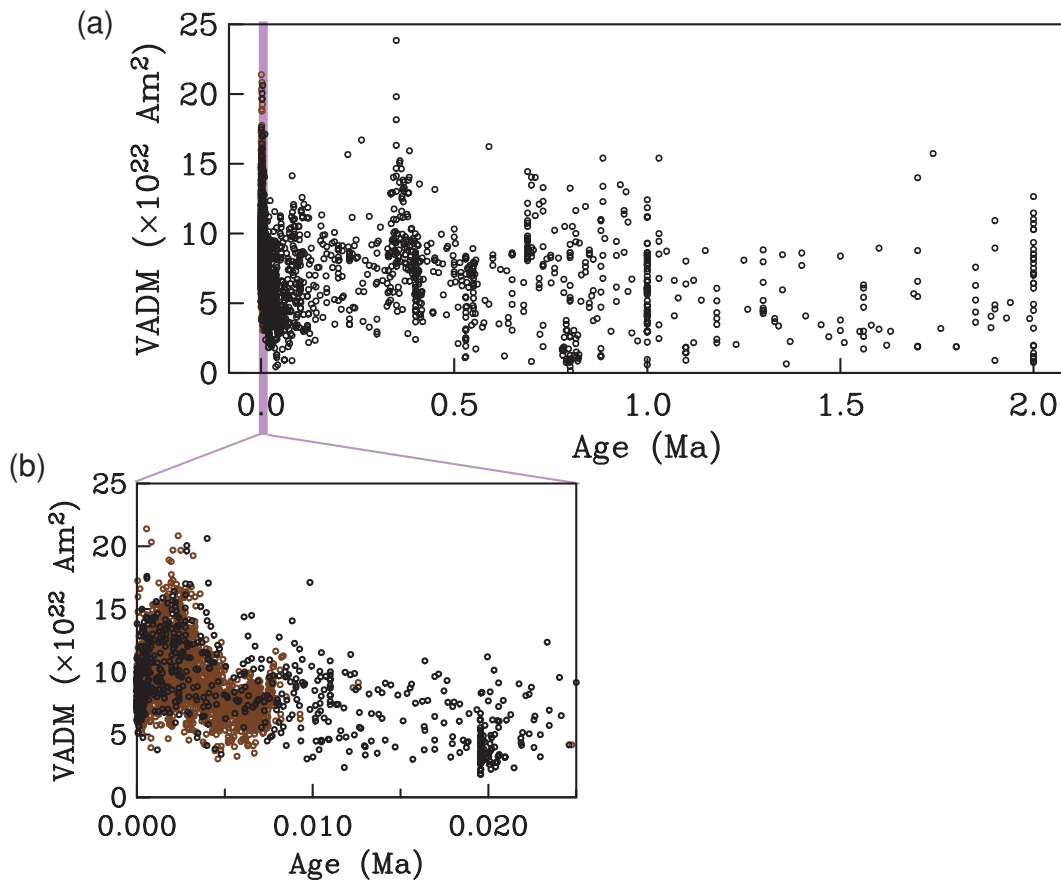


Figure 2. API data as a function of age. Black (brown) circles correspond to igneous (archaeological) sources. (a) 0–2 Myr; (b) 0–25 kyr.

Summary information for all 86 cores is given in Table 1, where for illustrative purposes and to guide our modelling, we have categorized the data into four sets corresponding to the colour and letter codes in Figs 1 and 3. The groups are as follows: nine P0 records, 34 Long Records (LR), 35 Young Records (YR) and eight records focused on the Brunhes/Matuyama Reversal (BM). P0 data all span more than 1.5 of the last 2 Myr and include the BM reversal. LR generally span several 100 kyr, but may begin at any age. YR are shorter records that do not extend past 250 ka in age. BM records are very short time-series developed for studying the BM reversal. In total, the records range from 19 kyr to 2 Myr in length providing variable coverage of the 0–2 Ma interval. Sedimentation rates range from 0.3 to 35 cm kyr^{-1} , which provides some idea of the variability in temporal resolution. The geographic distribution of cores is shown by the colour-coded triangles in Fig. 1. As with API data, the northern hemisphere data are more numerous, but there is a reasonable number of cores from the southern hemisphere. Fig. 3 gives a sense of the actual temporal coverage for the 0–2 Ma interval, plotting the age ranges spanned by each core (with each bar representing one core) along with a plot of the number of cores as a function of age.

The P0 time-series form the basis of our preliminary model PADM2Mp and are illustrated in Fig. 4, where the differences among the nine records make it clear that the data reflect more than a simple time-varying axial dipole. The challenge is to extract the PADM, which we first attempt with the P0 data alone and then with the entire set of 86 records. The results are described in Section 4, but first we motivate and describe the PML modelling algorithm.

3 A PML METHOD

In this section, we provide a brief rationale and description of the PML method that is the backbone of our modelling strategy for recovering the PADM. We refer those interested in the details of the algorithm to Appendix B.

From the previous section we abstract the concept of having two distinct kinds of data and a total of K distinct data series. Each series consists of distinct elements $d_{k,i}$, with subscript k , i referring to the i th point in the k th data set, where each set is either an RPI time-series from a specific location, or a collection of globally distributed API data. Our goal is to recover a time varying description of the PADM, here designated $v(t)$ and to outline a specific strategy to accomplish that. There are four aspects to this: (1) choosing a parametrization for $v(t)$; (2) using a misfit measure that accommodates the asymmetric noise distribution that is a perennial characteristic of VADM data; (3) recognizing that we want a model whose resulting temporal resolution and complexity is explicitly controlled by the inversion process rather than by the number of model parameters allowed and (4) including an implicit calibration of the RPI data.

The PML strategy that results is basically a merger of a maximum likelihood (ML) type estimation for parameters in non-Gaussian noise (Constable 1988) and a quadratic regularized inversion that penalizes roughness to provide a smoothly varying model as a function of time (Constable & Parker 1988; Parker 1994) with modifications to suit the specific noise distributions found in the 0–2 Ma VADM data and to accommodate the joint use of absolute and relative intensity data.

Table 1. Relative palaeointensity records used in PADM2M.

Core name	Lat. (°)	Lon. (°)	Min. age (ka)	Max. age (ka)	Sed rt. (cm kyr ⁻¹)	<i>n</i>	α, λ	Variance reduction (per cent)	References
P0 records									
ODP 983	61.4	-24.1	0	1888.9	16	16859	0.18, 2.06	22	1,2,3,4,5
ODP 984	60.4	-23.6	0	2151.9	12	16843	0.25, 2.21	32	2,4,5
ODP 1021	39.08	-126.22	13.4	1562.1	3	1869	0.50, 2.12	53	6,7
ODP 1010	29.97	-118.1	19.0	2036.0	1	1859	0.35, 1.62	30	6,8
MD97-2143	15.87	124.65	0	2140.0	2	1224	0.40, 1.77	37	9
MD98-2187	4.27	134.99	50.5	3052.7	1	831	0.32, 1.88	20	10
MD98-2185	3.08	134.99	8.9	2256.2	2	1605	0.44, 1.73	17	10
ODP 848-851	2	-110	33.5	4035.3	2.5	1312	0.19, 1.63	34	11
MD90-0940	-5.56	61.67	107.8	1954.4	<2	977	0.34, 1.50	21	12
Long records									
ps1852-2	70.26	-15.83	3.5	283.3	2	258	0.15, 1.30	12	13
ldb	45	4	19.45	307.57	15	428	0.22, 1.79	12	14,15
md95-2039	40.58	-11.00	29.6	317.4	7-25	1347	0.33, 1.62	23	16
md95-2040	40.58	-10.00	32.8	401.8	7-25	1409	0.22, 1.93	16	16
ngc69	40.00	175.00	6.87	883.02	1	229	0.48, 1.30	47	17
ded8708	39.37	13.34	39.5	405.6	10	192	0.22, 1.79	-1	18
su92-17	39.37	-26.60	4.4	280.0	2.4	690	0.57, 1.51	11	19
*lc07	38.15	10.07	754.0	1033.0	2.3	584	-	(-31)	20
su92-18	37.78	-27.22	4.4	280.0	3.5	690	0.26, 1.54	23	19
su92-19	37.3	-27.08	4.4	278.8	3	687	0.16, 2.26	21	19
ngc65	35.24	175.00	6.5	634.9	1	130	0.42, 2.49	35	17
rc10-167	33.03	150.38	10.7	781.1	2.1	722	0.34, 1.36	2	21
kk78-030	18.9	-160.3	601.3	1785.4	2	1636	0.22, 1.01	7	22
769	8.78	121.30	5.0	1106.0	8	719	0.46, 2.18	7	23,24
767	4.78	123.5	601.0	1518.2	10	530	0.22, 1.08	9	25,26
kh90-3-5	4.00	160.02	5.0	1106.0	1	1102	0.44, 1.69	37	27
807a	4.0	157.0	781.14	2036.4	-	475	0.14, 2.57	29	28
np35	3.80	141.49	126.7	697.9	1	221	0.39, 2.14	5	29
p226	2.88	-169.58	40.6	780.0	0.6	195	0.51, 1.76	20	29
kh73-4-7	2.69	164.84	2.0	1160.0	1	1159	0.33, 1.43	2	30
*803a	2.26	160.30	783.0	1396.0	1	1396	-	(-24)	28
803b	2.26	160.3	1487.9	2786.3	1	173	0.27, 1.38	-2	28
md97-2140	2.05	141.76	568.3	1465.1	1	680	0.14, 2.57	39	31
md98-2183	2.01	135.02	19.9	1193.0	2	3361	0.47, 1.55	30	10
rmdb75p	1.9	160.2	123.7	1193.0	1	795	0.40, 1.58	7	32
ngc36	1.22	160.57	0.8	546.0	1	106	0.36, 1.31	12	29
kh73-4-8	-1.55	167.64	36.0	1160.0	1	1125	0.35, 1.39	27	30
*e113p	-1.64	159.22	4.4	379.6	1.3	557	-	(-63)	33
kr9912-pc5	-9.35	-162.83	1294.5	2117.7	0.3-1.5	260	0.37, 1.40	-4	10
*kr9912-pc2	-10.75	-163.49	1003.9	2999.2	0.3-1.5	980	-	(-15)	10
ngc38	-14.99	175.16	9.5	405.5	1	71	0.36, 1.31	46	29
*ks87-752	-37.75	-38.05	600.4	1022.6	-	283	-	(-29)	34
*1089	-40.94	9.89	20.1	578.3	15-20	8073	-	(-56)	35
1101	-64.37	-70.27	706.3	1105.0	7	800	0.30, 1.47	17	36
Young records									
ps2644-5	67.87	-21.77	11.5	76.0	37	636	0.33, 1.48	30	37,38
md95-2009	62.74	-3.99	10.3	76.0	33	648	0.42, 2.53	34	37,38
su90-24	62.67	-37.38	11.0	76.0	32	641	0.23, 3.07	17	37,38
su90-33	60.57	-22.09	11.5	76.0	11	636	0.23, 1.19	2	37,38
ver98-1-6	53.69	108.35	64.5	234.5	4.3	356	0.35, 2.71	4	39
305-a5	53.0	106.0	0.4	10.8	12	27	0.35, 2.71	22	40
BaikalStack	53.0	106.0	12.8	83.8	12	199	0.35, 2.71	28	40
884	51.45	168.34	16.2	210.0	5	864	0.32, 2.57	37	41
883	51.20	167.77	16.2	210.0	5	863	0.32, 2.57	37	41
882b	50.36	167.60	0.9	204.9	4	63	0.32, 2.57	31	42
*md95-2024	50.20	-45.69	1.5	117.0	22	2407	-	(-9)	43
su9003	40.51	-32.05	7.3	231.6	5	617	0.33, 1.18	24	44
ket8251	39.48	14.17	7.9	95.2	5	71	0.22, 1.79	12	18
ded8707	39.41	13.35	9.8	59.7	10	192	0.22, 1.79	30	18
md01-2440	37.8	-10.0	2.2	54.5	15-35	304	0.20, 1.91	8	16

Table 1. (Continued.)

Core name	Lat. (°)	Lon. (°)	Min. age (kyr)	Max. age (kyr)	Sed rt. (cm kyr ⁻¹)	<i>n</i>	α, λ	Variance reduction (per cent)	References
*md01-2441	37.8	-10.0	28.5	53.7	15–35	301	–	(–17)	16
md95-2042	37.8	-10.0	31.7	160.9	15–35	399	0.29, 1.70	13	16
*md99-2334	37.8	-10.0	0.2	37.6	15–35	236	–	(–38)	16
md84-629	36.04	33.08	15.5	58.6	12	201	0.28, 2.01	26	18
md95-2034	33.69	-57.58	11.5	76.0	40	636	0.22, 1.19	2	37,38
ch88-10p	29.0	-73.0	14.2	67.8	22	315	0.40, 2.14	5	45
Sed-17aK	25.28	-17.11	8.4	223.8	4–13	344	0.20, 1.91	10	46
768a	8.0	121.22	5.1	94.2	10	73	0.42, 1.97	34	24
768b	8.0	121.22	9.3	130.3	10	105	0.42, 1.97	20	24
*md98-2181	6.30	125.83	11.8	65.7	45	514	–	(–6)	47
ngc29	4.13	136.27	2.3	192.1	1–10	74	0.28, 1.83	49	48
md85-674	3.19	50.44	18.2	138.3	10	284	0.26, 1.25	35	49
ngc26	3.00	135.02	1.2	119.7	1–10	74	0.28, 1.83	44	48
md85-669	2.49	46.92	20.1	138.0	5	239	0.20, 1.20	22	49
ngc16	2.00	135.00	1.6	191.2	1–10	125	0.28, 1.83	30	48
np7	2.00	138.01	5.7	199.4	1–10	70	0.28, 1.83	41	48
np5	1.01	136.96	8.5	196.4	1–10	132	0.28, 1.83	23	48
md85-668	-0.02	46.04	20.9	187.3	5	191	0.29, 1.36	14	49
21-pc02	-41.14	7.81	0.5	80.7	13.5	1450	0.44, 2.19	39	35,50,51
md84-528	-42.11	53.04	15.6	94.0	12	927	0.36, 1.43	10	18
BM reversal records									
609b	49.86	-24.23	777.1	824.9	7	176	0.28, 1.30	62	52
606a	37.00	-37.00	773.0	792.0	–	70	0.28, 1.30	7	53
767b	4.78	123.5	758.8	828.8	8	58	0.28, 1.30	19	25,26
665a	3.0	-20.0	770.3	817.3	4	38	0.28, 1.30	47	52
805b	1.14	160.32	769.8	820.8	2	40	0.28, 1.30	45	52
804c	1.0	161.4	774.0	796.0	1	22	0.28, 1.30	41	52
664d	0.1	-23.27	769.8	806.7	4	73	0.28, 1.30	43	54
v16-58	-46.5	31.3	766.5	789.6	<2	56	0.28, 1.30	10	55,56

** Core is excluded from final model; *n* is number of data used from RPI record; α, λ are the two best fitting APD pdf shape parameters for the residuals distribution.

References: 1, Channell *et al.* (1997); 2, Channell (1999); 3, Channell & Kleiven (2000); 4, Channell *et al.* (2002); 5, Channell *et al.* (2004); 6, Leonhardt *et al.* (1999); 7, Guyodo *et al.* (1999); 8, Hayashida *et al.* (1999); 9, Horng *et al.* (2003); 10, Yamazaki & Oda (2005); 11, Valet & Meynadier (1993); 12, Meynadier *et al.* (1994); 13, Nowaczyk & Frederichs (1999); 14, Williams *et al.* (1998); 15, Thouveny *et al.* (1994); 16, Thouveny *et al.* (2004); 17, Yamazaki (1999); 18, Tric *et al.* (1992); 19, Lehman *et al.* (1996); 20, Dinares-Turell *et al.* (2002); 21, Kent & Opdyke (1977); 22, Laj *et al.* (1996); 23, Schneider (1993); 24, Schneider & Mello (1996); 25, Guyodo & Valet (2006); 26, Schneider *et al.* (1992); 27, Sato *et al.* (1992); 28, Kok & Tauxe (1999); 29, Yamazaki & Ioka (1995); 30, Sato & Kobayashi (1989); 31, Carcaillet *et al.* (2003); 32, Tauxe & Shackleton (1994); 33, Tauxe & Wu (1990); 34, Valet *et al.* (1994); 35, Stoner *et al.* (2003); 36, Guyodo *et al.* (2001); 37, Kissel *et al.* (1999); 38, Laj *et al.* (2000); 39, Oda *et al.* (2002); 40, Peck *et al.* (1996); 41, Roberts *et al.* (1997); 42, Okada (1995); 43, Stoner *et al.* (2000); 44, Weeks *et al.* (1995); 45, Schwartz *et al.* (1996); 46, Haag (2000); 47, Stott *et al.* (2002); 48, Yamazaki & Ioka (1994); 49, Meynadier *et al.* (1992); 50, Stoner *et al.* (2002); 51, Channell *et al.* (2000); 52, Hartl & Tauxe (1996); 53, Clement & Kent (1986); 54, Valet *et al.* (1989); 55, Clement & Kent (1991) and 56, Kent & Schneider (1995).

3.1 Cubic B-spline parametrization

Following a strategy widely used for time-varying spherical harmonic models of the geomagnetic field (Bloxham & Jackson 1992; Jackson *et al.* 2000; Korte *et al.* 2009) we write the time-varying PADM, $v(t)$, as a linear combination of p cubic B-splines,

$$v(t) = \sum_{j=1}^p \beta_j c_j(t), \quad (1)$$

where $c_j(t)$ are cubic B-spline basis functions evaluated at time t and β_j are the corresponding coefficients. We describe our observations ($d_{k,i}$) at time $t_{k,i}$ as the sum of the model plus a noise term ($\epsilon_{k,i}$), incorporating the scaling of RPI records as follows,

$$\zeta_k d_{k,i} = v(t_{k,i}) + \zeta_k \epsilon_{k,i} \quad (2)$$

$$= \sum_{j=1}^p \beta_j c_j(t_{k,i}) + \zeta_k \epsilon_{k,i}, \quad (3)$$

where ζ_k , $k = 1, \dots, K$ provides the scaling factor needed to calibrate the k th RPI data series into pseudo-absolute VADMs. In the case of API data $\zeta_k = 1$ if the data are expressed as VADMs.

3.2 Non-Gaussian noise

When designing or choosing a modelling method, we first need to consider the noise distribution of the data, the statistics of the $\epsilon_{k,i}$. In the case of palaeointensity data, the distribution function associated with data noise is unknown—although often implicitly assumed to be Gaussian or at least symmetric. The noise associated with VADM data arises from multiple sources including: natural variations inherent to the data materials, uncertainties associated with lab measurements and contributions associated with local non-axial-dipole field features that are carried along in translating palaeointensities into VADMs. None of these noise sources can be assumed Gaussian, not least because the scalar palaeointensities themselves are bounded below at zero, and the noise may reflect this asymmetry. In Appendix A, we show that the

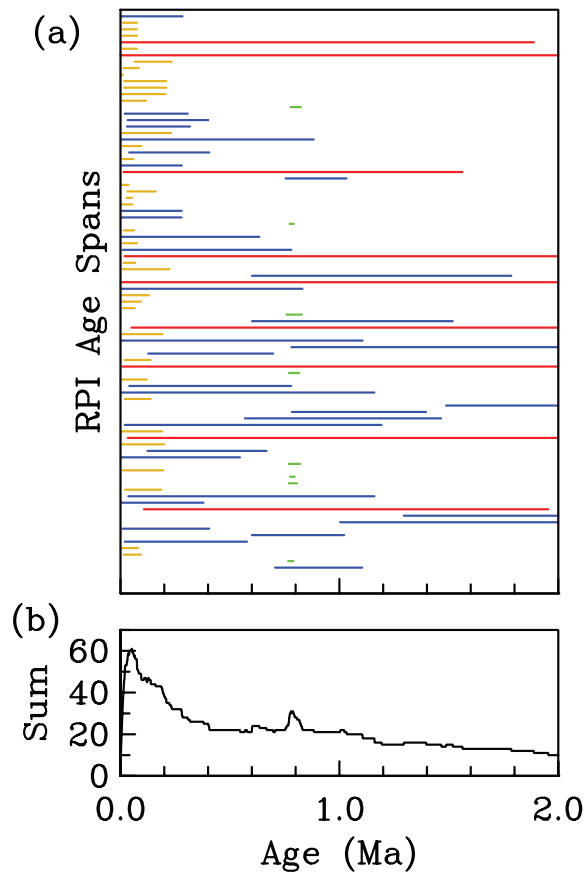


Figure 3. Age spans of RPI records, colours as in Fig. 1 (red, blue, yellow and green correspond to P0, Long, Young and Reversal records, respectively). (a) Each bar corresponds to age span of one RPI time-series. Names of cores are omitted, but cores are plotted by latitude, with highest latitude records at the top and decreasing toward the bottom. (b) Total number of RPI time-series at each age.

expected distribution is non-Gaussian and this introduces bias to estimates of PADM derived by the standard strategies of stacking and averaging multiple RPI records. This bias is in part a consequence of using the scalar intensities only instead of the complete vectors when studying the magnetic field and is consistent with the conclusion of Love & Constable (2003) who found that an arithmetic mean of intensity data does not correspond to the intensity of the mean field vector.

As an illustration of asymmetry in VADM data that can lead to bias in PADM estimates, consider the 2005 magnetic field as represented by the International Geomagnetic Reference Field (IGRF 2005) [http://www.ngdc.noaa.gov/AGA/vmod/igrf.html, Maus *et al.* (2005)]. We manufactured a data set of field magnitudes at globally distributed locations and then convert these into VADMs. If the noise were Gaussian, the true axial dipole moment would be best estimated by taking the mean of the data. However, the resulting distribution shown in Fig. 5(a) is non-Gaussian and quite asymmetric. In this case, a simple average of the data produces a mean field strength estimate of $8.1 \times 10^{22} \text{ Am}^2$, while the true axial dipole moment is $7.6 \times 10^{22} \text{ Am}^2$. A better estimate of the axial dipole moment would be the mode of the distribution ($\sim 7.8 \times 10^{22} \text{ Am}^2$). While this particular distribution is strongly influenced by the spatial structure of the non-axial-dipole field of IGRF 2005, the skew seen here is a feature also seen in data sets which span long

periods of time. For example, a skewed distribution and corresponding bias in the mean was noted for 0–5 Ma VADMs by McFadden & McElhinny (1982). The distributions associated with the data in Fig. 4 are also long-tailed on the positive side (see Fig. 5b). Our modelling procedure (described below), estimates the noise distributions of palaeointensity data empirically using the residual distributions after model fitting. Residual distributions of the data in Fig. 4 for the final PADM2M model are plotted in Fig. 5(c) along with a representative normal distribution. They clearly depart from a normal distribution.

The asymmetry also means that the usual least squares measure of misfit is inappropriate when modelling these data. Alternatively, ML methods will generally give asymptotically unbiased, efficient parameter estimates (Rice 1995) and can be a better alternative to parameter estimation when noise is known to be non-Gaussian (or when one wants to avoid making this assumption). We therefore develop a maximum likelihood approach to our PADM modelling.

3.3 ML methods

As mentioned above, we parametrize the time-varying PADM with cubic B-splines and build on ML fitting methods developed by Constable (1988). There, an ML-type method is used to find a best fitting set of model parameters, where these parameters are coefficients β_j , $j = 1, \dots, p$ for a set of basis functions (in our case, cubic B-splines). When the noise distribution is known the solution to the non-linear ML problem is reframed in the form of an iteratively reweighted least-squares problem, which is solved using one of a number of readily available computational tools [see Press *et al.* (1986)]. Constable (1988) proposed that when the probability density function (pdf) for the noise is not known *a priori*, it can be estimated iteratively from the residuals to a best fitting model provided there are sufficient data. In the original formulation, the determination of the pdf was completely empirical and non-parametric (as in Fig. 5a, for example), but here we adopt a simple parametric model for the pdf of the noise. We use the best fitting asymmetric power distribution (APD) pdf (Komunjer 2007) which has two shape parameters, a location parameter, and a scaling parameter to describe the distribution of the residuals. Fig. 6 illustrates the broad range of potential APD pdf shapes; a mathematical definition is provided in Appendix B. Both the previous non-parametric estimation and the new APD pdf estimation have the flexibility to take on a variety of shapes to fit the unknown noise distribution. However, estimating the pdf of the noise parametrically streamlines the whole fitting routine significantly. The broad range of available APD shapes allows us to accommodate different noise distributions for each of the K time-series.

Once the pdf is estimated it is straightforward to recast the ML optimization criteria in the form of an iteratively reweighted least squares problem and find parameter estimates which maximize the probability of getting the data observed. The method is elaborated in Appendix B, but briefly we note that to find a spline model for a single data series of length n_k with noise pdf $f_k(x)$ we would use the following strategy.

The function to be maximized in this case, the likelihood function, $L_k(\hat{\beta})$, is the joint pdf, F_k , of the sample errors, which is in turn the product of the pdfs evaluated at the ML estimate of the parameters $\hat{\beta}$. If the residuals are independent, identically distributed (i.i.d.)

$$L_k(\hat{\beta}) = F_k(\epsilon, \hat{\beta}) = \prod_{i=1}^{n_k} f_k(\epsilon_i, \hat{\beta}). \quad (4)$$

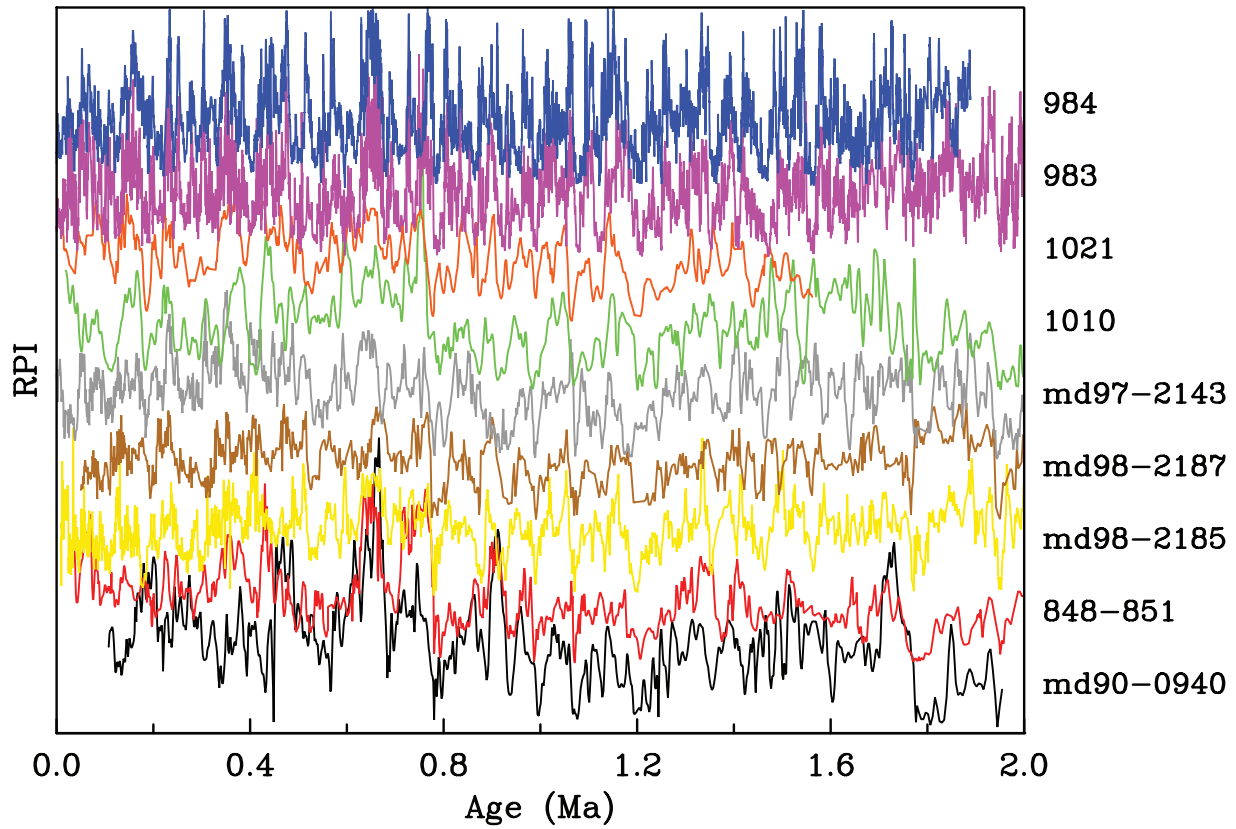


Figure 4. P0 RPI records, plotted as RPI versus age, where each record has a mean of one (offset between records for visual clarity only). Names of cores on right axis.

As is generally done, in practice we minimize the negative log likelihood ($l_k(\hat{\beta})$), so that the product becomes a sum making the problem more tractable

$$l_k(\hat{\beta}) = \sum_{i=1}^{n_k} \rho_k(\epsilon_i), \quad (5)$$

where $\rho_k(\epsilon) = -\ln[f_k(\epsilon, \hat{\beta})]$ and is termed the loss function.

For the K data sets, minimizing with respect to the model parameters $\hat{\beta}$ and reframing as an iterative weighted least squares problem yields the set of equations

$$\frac{\partial l}{\partial \beta_j^q} = \sum_{k=1}^K \sum_{i=1}^{n_k} w_{k,i}^q c_j(t_{k,i}) \left(\tilde{d}_{k,i} - \sum_{j=1}^p \beta_j^q c_j(t_{k,i}) \right) = 0 \quad (6)$$

$$w_{k,i}^q = N_k^{q-1} C_k^{q-1} \left| \tilde{d}_{k,i} - \sum_{j=1}^p \beta_j^{q-1} c_j(t_{k,i}) \right|^{D_k^{q-1}} \quad (7)$$

$$\tilde{d}_{k,i} = \zeta_k d_{k,i} - \mu_k^{q-1}. \quad (8)$$

The weights used in the q th iteration involve residuals from the previous $(q-1)$ th model iteration and factors derived from the noise pdf parameters estimated from those residuals [here labelled C_k^{q-1} and D_k^{q-1} , but explicitly defined in Appendix B, eqs (B20)–(B22)]. In the case written above, a distinct noise pdf is calculated for each of the k data series (giving k distinct values of C and D). However, we

can also group data sets together under the same noise distribution if that is appropriate. For ease of notation we refrain from writing that out explicitly, but note here that we often group very short RPI data with others from similar geographic regions to provide enough data points for a more robust estimate of the pdfs. The weights also incorporate a normalization factor (N_k^{q-1}) used to account for the size of the k th data set, so that each data set (regardless of size) contributes equal weight over any specific time interval in the minimization.

3.4 Penalizing the ML method

We have not yet dealt with the question of how to choose p , the number of B-spline parameters. We follow the strategy outlined as item (3) at the beginning of Section 3, recognizing that we want a model whose resulting temporal resolution and complexity is explicitly controlled by the inversion process rather than by the number of model parameters allowed. Framed this way, we choose p to be large, then combine the ML method outlined above with the regularized weighted least squares cubic B-spline model fitting routine developed in Constable & Parker (1988), which penalizes the model roughness, $R(\hat{\beta})$, for the PADM, $v(t)$. $R(\hat{\beta})$ is specified in terms of the integrated squared second derivative of the resulting model

$$R(\hat{\beta}) = \int_{t_1}^{t_n} \left[\partial_t^2 \sum_{j=1}^p \beta_j c_j(t) \right]^2 dt. \quad (9)$$

A trade-off parameter, Λ , controls the balance between minimizing roughness and minimizing the loss function ρ_k defined in the

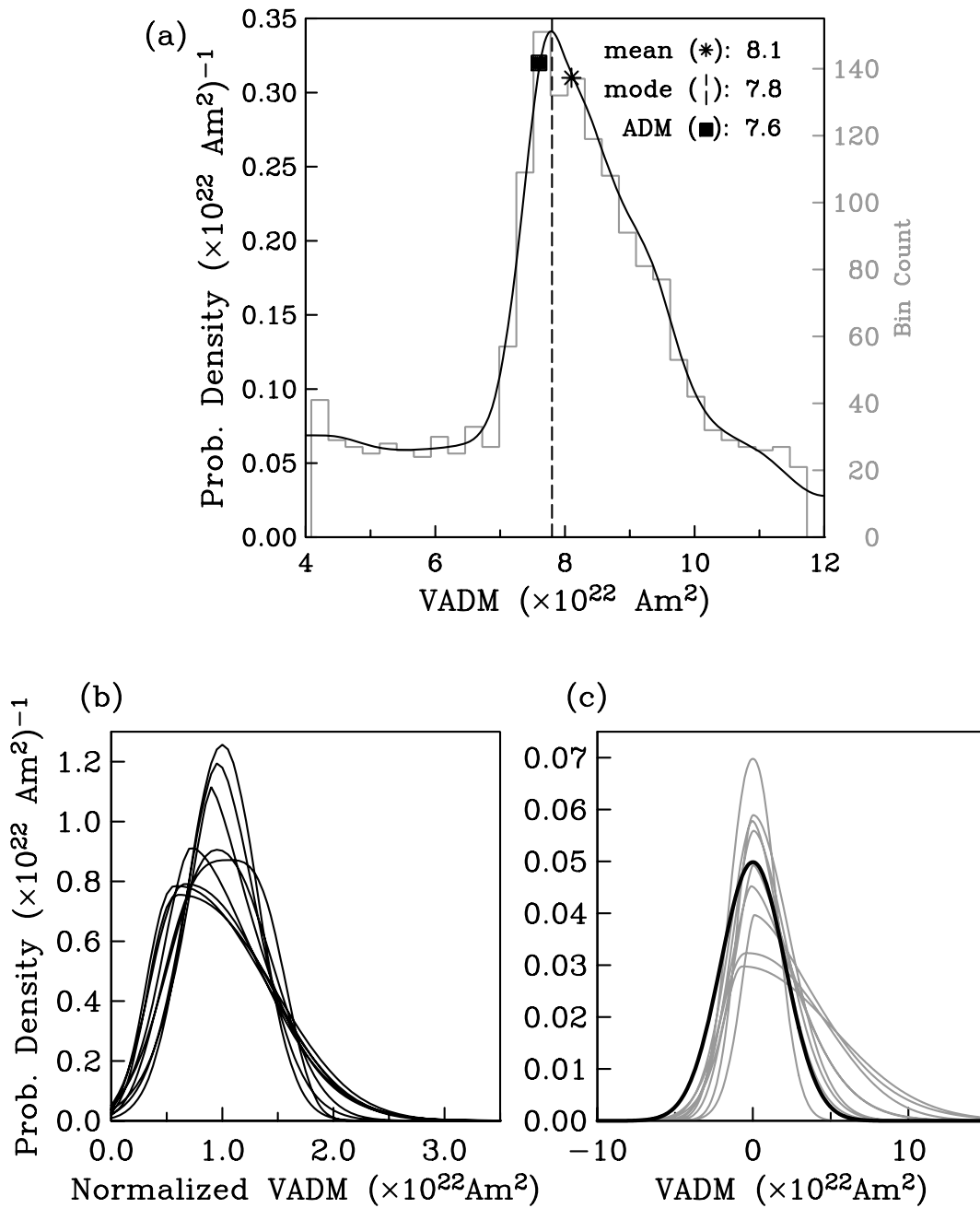


Figure 5. (a) Histogram (grey) and pdf (black) of VADMs from the IGRF 2005 field model at a grid of globally distributed locations. Black square corresponds to the true axial dipole moment (from g_1^0), dashed line and asterisk correspond to the mode and mean of the distribution, respectively. (b) RPI pdfs for the nine P0 records, expressed in terms of VADM with a normalized mean of one. (c) Residual distributions (after PADM2M model fit) for the nine P0 records (grey) along with a normal distribution (black) with a mean of 0 and a variance intermediate of the residual distributions for reference.

previous subsection. This adds in the penalty part of the PML algorithm. The resulting objective functional to be minimized over β and Λ is

$$U(\beta) = l_k(\beta) + \Lambda R(\beta). \quad (10)$$

The approach advocated by Constable & Parker (1988) for penalized splines and by Constable *et al.* (1987) for analogous non-linear problems to solve for Λ generally supposes that the likelihood function corresponds to that expected for normally distributed uncertainties and an associated expected value for the rms misfit which is χ^2

distributed. A side constraint is imposed with

$$[l_k(\beta)] = T$$

with T chosen so that for misfit normalized by uncertainty the expected value of the misfit corresponds to that for the χ^2 distribution when the data uncertainties are independently and identically Gaussian distributed. Here we have a more complex likelihood function associated with the APD pdfs and knowledge of the relative uncertainty of the various data contributions may be derived empirically during the fitting procedure. A more robust approach to determining a suitable value for Λ is on the basis of recovering an appropriate

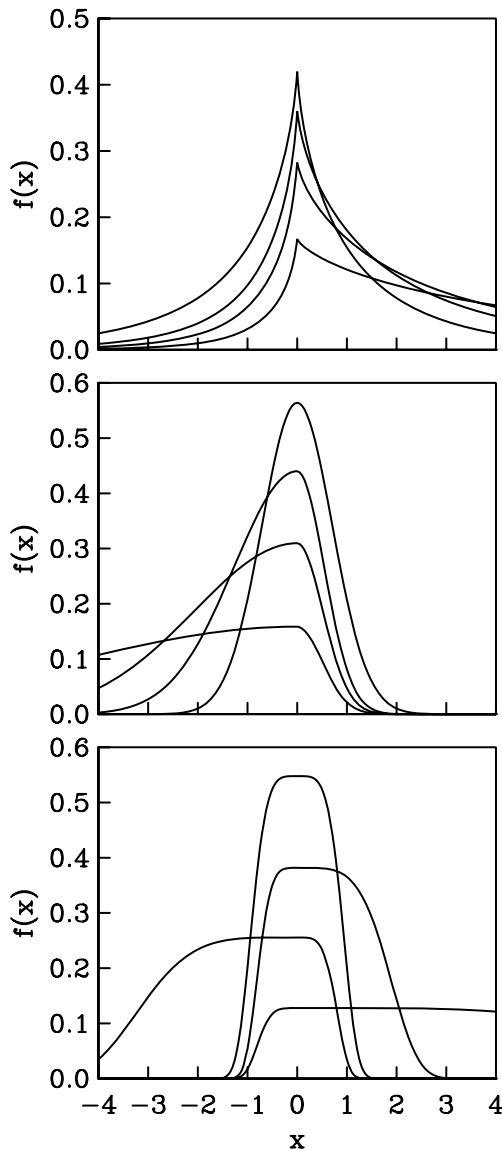


Figure 6. Example APD pdfs for an array of shape parameters (see text, Appendix B). $\mu = 0$, $\sigma = 1$ in all cases. (top panel) $\lambda = 0.75$, $\alpha = 0.1, 0.2, 0.3, 0.5$ (middle panel) $\lambda = 2$, $\alpha = 0.5, 0.7, 0.8, 0.9$ (bottom panel) $\lambda = 4.5$, $\alpha = 0.1, 0.3, 0.5, 0.7$.

frequency resolution for the model. This is not an arbitrary choice but draws on relevant literature which investigated the reliability of RPI records, especially given their age uncertainties, to choose an appropriate target resolution for our model. A visual inspection of the frequency spectrum of the model is used to settle on a value of Λ and corresponding value of T which gives the target resolution.

3.5 The complete algorithm

The flowchart in Fig. 7 shows the complete iterative PML algorithm. First, we fit a low-resolution penalized spline model to the sparse API data using a two-norm or regular least squares misfit measure (PLS spline in Fig. 7). We use this to predict a PADM value at every time point where we have RPI data, then estimate the scale (ζ_i) needed to transform each RPI series into pseudo-absolute VADMs. From there, we solve the PML equations above, where the 0th iteration is a Least Squares fit to find an initial set of residuals from

which pdf parameters and new PML weights can be estimated. We then iteratively find residuals, noise pdfs, weights and updated models until the model stops changing significantly (in practice, we iterate five times at which point the model norm changes less than 1 per cent). Note that each updated PML model is regularized and the trade-off parameter needed for a target misfit is also estimated through an iterative process as in Constable & Parker (1988). At that point we have the option of recomputing the scale values using the updated PML model and rerunning the PML fitting routine with the updated scale values. Rescaling once or twice is often useful since the initial scales are calculated from a low resolution model, which may not provide an adequate initial estimate for the true VADM. We note that there is no guarantee of convergence in the scaling procedure, but in practice this has not been a problem.

4 RESULTS

We apply the PML algorithm to the API data and to two compilations of RPI data and generate two distinct models, PADM2Mp and PADM2M, which are compared before we turn to a more general discussion. In both cases, we treat API data from igneous and archaeological sources as data sets with distinct noise distributions because Ziegler *et al.* (2008) found that these data types were statistically different and have differing temporal distributions and resolutions.

For each model we specify up front the density of spline knot points, the target misfit and the maximum number of iterations for (i) scale value estimation (ii) noise distribution estimation and (iii) trade-off parameter estimation. The appropriate number of iterations involved in estimating the trade-off parameter and noise distributions is straightforward (we iterate five times in each case). We rescale twice for reasons discussed in Section 3.5. Both models are made using 2000 knot points (1 per kyr), providing a sufficient number of parameters to ensure that the temporal resolution is controlled by the regularization. The regularization needed is specified by the target misfit, T , and is less obvious. We turn to the frequency domain to address this issue. McMillan *et al.* (2002) showed that due to age uncertainties in sediments, intensity variations on timescales less than 10 kyr are difficult to resolve from this data source. We therefore choose the amount of regularization (through Λ) in each case which suppresses energy at timescales of 5–10 kyr (frequencies less than 100–200 Myr⁻¹), and judge from the power spectrum of the resulting model that this is criterion is met. Since the value of Λ in eq. (10) needed to meet this criterion is not known *a priori*, we look at a range of models incorporating differing levels of smoothing and their power spectra (not shown here) to choose the most appropriate regularization parameter.

The first model discussed, PADM2Mp, is a preliminary model using only nine of the available RPI time-series (Section 4.1). The second, PADM2M, is our preferred model from a more complete set of RPI records (Section 4.2). Both are plotted in Fig. 8 and discussed later.

4.1 PADM2Mp

PADM2Mp is a preliminary time-varying, 0–2 Ma PADM model created using the P0 subset of nine globally distributed RPI data sets (see Table 1), together with the PINT08 and Geomagia50 API data sets. These RPI records, already shown in Fig. 4, each span more than 1.5 Myr, and have significant amounts of data both before and after the BM reversal. They provide a good starting point for using

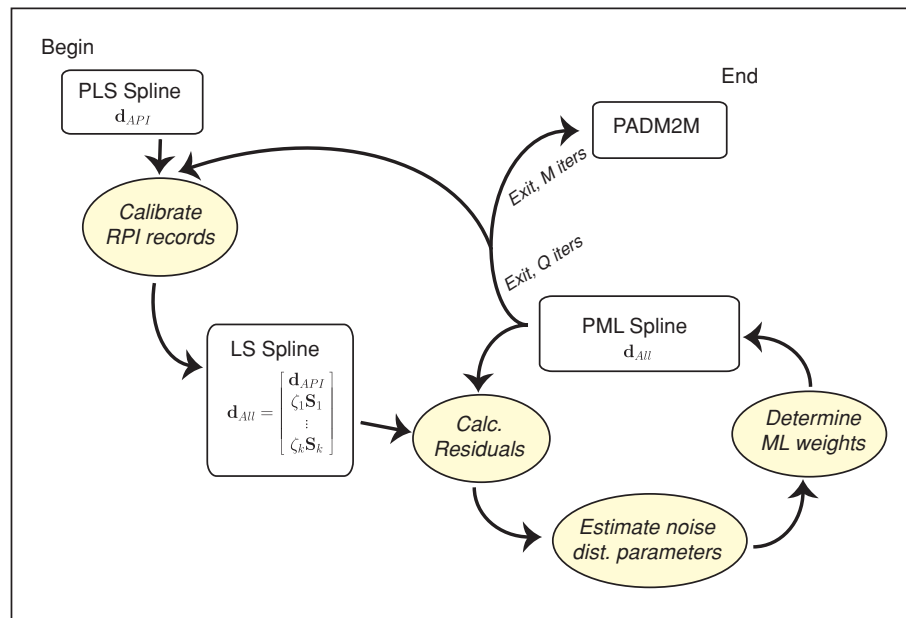


Figure 7. Flowchart of computational algorithm used in this study. See text, Section 3.5 for details.

the PML algorithm on a real data set, characterizing uncertainties in the model and comparing features of the Brunhes and Matuyama chrons (Section 5).

PADM2Mp is shown in red in Fig. 8 and shows the expected lows at field reversals and excursions and estimates the current field strength to within 1 per cent [$\nu(0) = 7.55 \pm 0.09 \times 10^{22} \text{ Am}^2$, where the true value is $7.6 \times 10^{22} \text{ Am}^2$]. Uncertainties have been estimated using a delete-1 jackknife procedure, where we recreate a model nine times leaving out one of the nine RPI records each time. The PADM2Mp uncertainties plotted in Fig. 8 are the minimum and maximum value of the suite of jackknife models at any given time. Uncertainties quoted are $\pm 2\sigma$ of the values instead of the minimum and maximum. The uncertainties illustrate both the consistency of the data sets and that PADM2Mp is not predominantly controlled by any one data set. The areas of highest variability are in sections of the model older than 1.5 Myr.

We evaluate the effectiveness of our modelling by calculating the variance reduction for each data set individually and find that values for the RPI series range from 21 to 42 per cent and the PINT08 and Geomagia50 API data sets have variance reductions of 34 and 30 per cent, respectively. Variance reduction is limited by poor age controls for some data and by high resolution signal recorded in data but inaccessible in million year field modelling.

PADM2Mp successfully shows the viability of PML modelling. We turn now to a model using all available information.

4.2 PADM2M

We created a model using our PML routine, the PINT08 and Geomagia50 API data and 86 RPI records from the compilation discussed in Section 2. After obtaining an initial model using this data set, we found that 10 RPI series have negative variance reduction (i.e. there is more variance in the residuals after a fit than in the raw data), indicating that these data series are incompatible with the model. These RPI records, discussed further in Section 5, are marked with an asterisk in Table 1 and are eliminated from our preferred model.

The remaining 76 RPI records and API data are used to produce PADM2M (Palaeomagnetic Axial Dipole Moment for

0–2 Ma). The model provides a reasonable fit to the data, with variance reductions of 31 and 24 per cent for PINT08 and Geomagia50 data sets, respectively, and variance reductions ranging from –4 to 62 per cent for the RPI data sets, with a median of 22 per cent. Three more RPI records have a slightly negative variance reduction after the fit to 76 records, but we refrained from iterating the process of trimming data and refitting. Variance reduction for all RPI data are listed in Table 1 for reference. For the 10 records eliminated from the final model, the variance reduction listed in parenthesis is in relation to the 86 record model. The range of agreement between the model and individual RPI data sets reflects RPI quality, but also differences in temporal resolution between the model and each time-series. Uncertainties are found in the same manner as described for PADM2Mp.

PADM2M reproduces the current field to within 1 per cent [$\nu(0) = 7.55 \pm 0.05 \times 10^{22} \text{ Am}^2$] and shows intensity lows at reversals and excursions (Fig. 8). While incorporating a much larger data set, PADM2M generally agrees with the preliminary model made from only nine LR at most time periods. The most notable difference occurs between approximately 600 and 700 ka, where an intensity peak seen in PADM2Mp is muted in PADM2M. The larger global compilation of 23 records used in PADM2M should give a more reliable result than the subset of nine used in PADM2Mp. In the youngest part of the models (<100 ka), where PADM2M adds many tens of RPI series, there are also some moderate differences between the preliminary model and PADM2M.

5 DISCUSSION

5.1 Comparison to VADM models

In Fig. 9, we compare PADM2M with two published VADM models, Sint-2000 (Valet *et al.* 2005) and PISO-1500 (Channell *et al.* 2009). PISO-1500 is a scaled stack of 13 RPI records. Sint-2000 is a composite of a 33 RPI series stack (0–800 ka) and a 10 RPI series stack (800–2000 ka). PISO-1500 has a notably different variance and resolution from Sint-2000 and PADM2M (Fig. 9) because it is constructed from RPI records of higher sedimentation rates. All

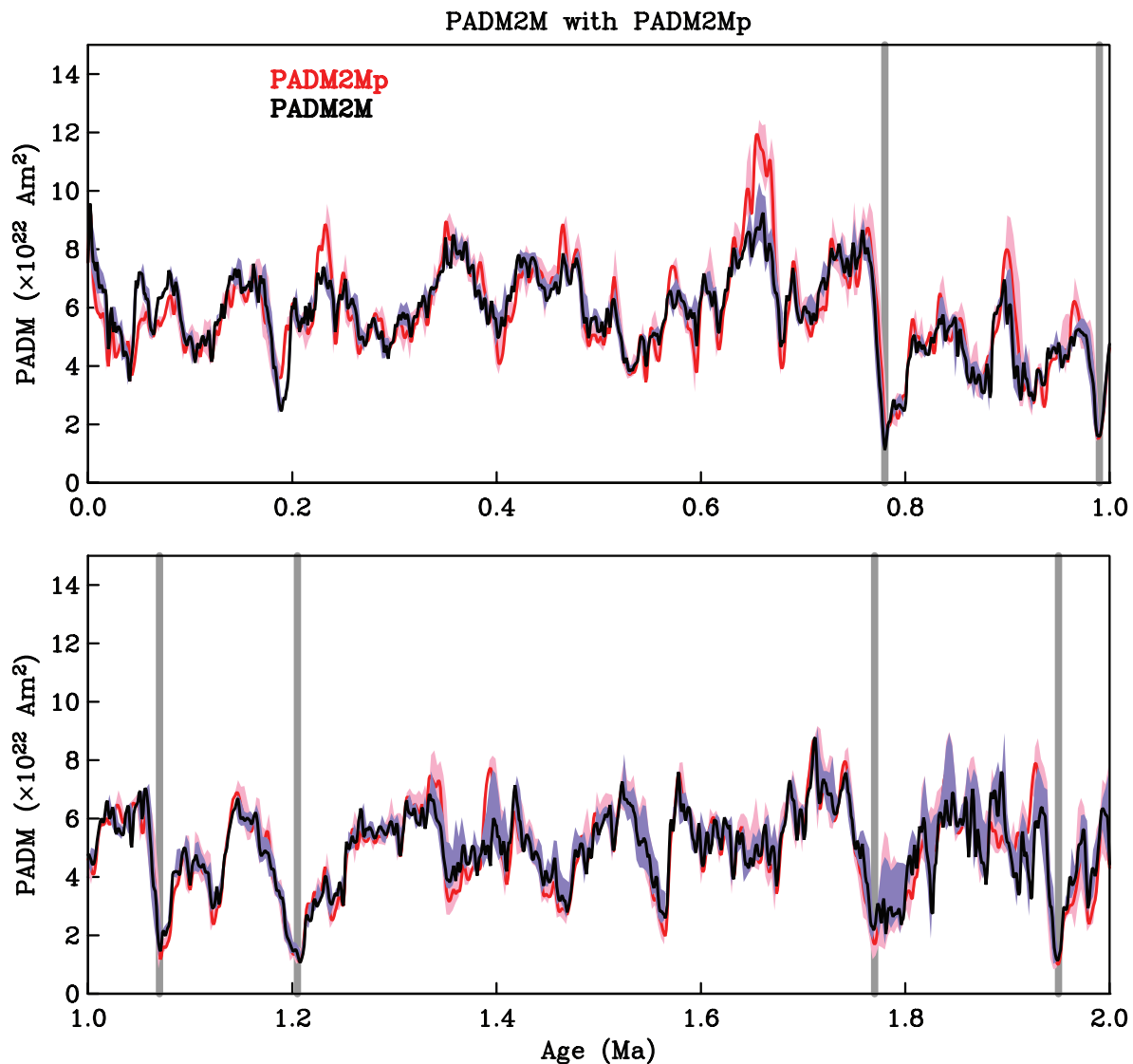


Figure 8. PADM2Mp model (red), made from a subset of nine RPI time-series and API data. Pink shading represents upper and lower jackknife bounds on PADM2Mp (see text). PADM2M in black, with bounds in blue-grey shading. Grey bars indicate known reversals. (Top-panel) 0–1 Ma. (Bottom-panel) 1–2 Ma.

models show lows at reversals and excursions and share similar long-period behaviour, but with a few differences.

In comparison to Sint-2000, and particularly in the Brunhes chron, PADM2M tends to peak at lower amplitudes. This is in part because our PML method addresses and, unlike the VADM stacks, accounts for bias in VADM data. From 600 to 700 ka, where PADM2M and PADM2Mp disagree most, both Sint-2000 and PISO-1500 show the more pronounced peak in field strength seen in PADM2Mp. For this time period, PADM2M incorporates more than twice as many RPI records as the Sint-2000 and PISO-1500 stacks (23, 10 and 6 RPI records used, respectively). For this particular feature, the amplitude difference is due both to our PML method and to PADM2M's incorporation of a larger global data set.

In the older part of the models (>1.3 Ma) the timing of some features differ among Sint-2000, PISO-1500 and PADM2M. We note that PADM2M uses published age models for most RPI data, except for some minor age recalibrations to use consistent ages for reversal boundaries (see Section 2). Sint-2000 correlates some intensity minima before stacking (Valet *et al.* 2005) and PISO-1500

uses the Match protocol of Lisiecki & Lisiecki (2002) to correlate intensity and oxygen isotope information before stacking. The timing differences reflect these methodology differences. We prefer to avoid geomagnetic tuning, so that our age scale is independent of RPI data.

Finally, because the other models are made from RPI data only (which weakly constrain the most recent field behaviour because tops of cores are often missing or damaged in the coring process) and PADM2M incorporates well-dated recent API data, PADM2M is better suited to recover estimates of the current field strength. PISO-1500 does not model 0–5 ka field strength; Sint-2000 does not model 0–1 ka and has a low VADM of $4.8 \times 10^{22} \text{ Am}^2$ for $t = 1 \text{ ka}$, but has more reasonable field values starting at 2 ka.

5.2 Statistical analysis of PADM2M

Table 2 gives some statistics of PADM2M, including the mean and standard deviation of the full 0–2 Ma model, the Brunhes chron, and the Matuyama chron younger than 2 Ma. PADM2M has a mean

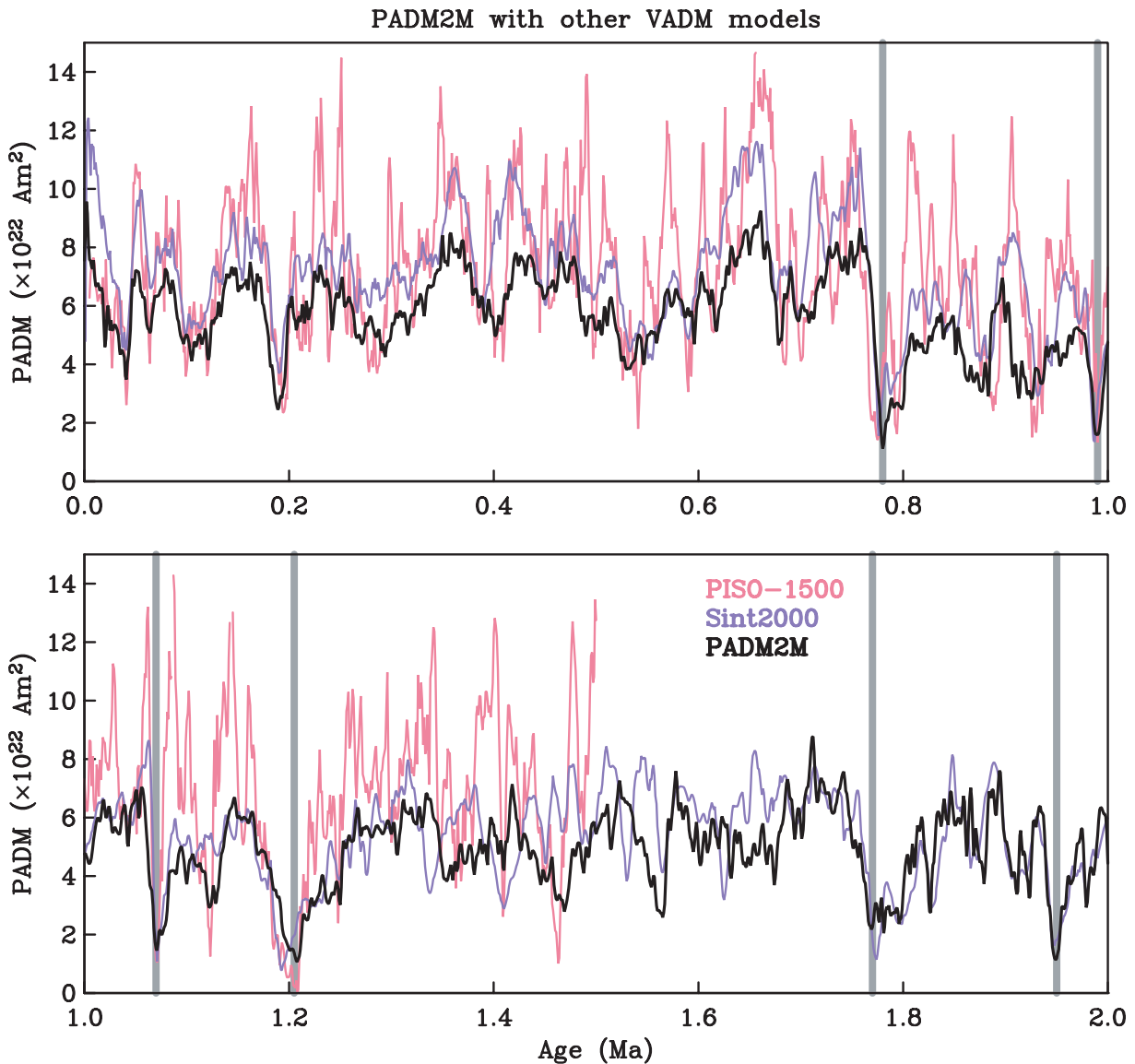


Figure 9. PADM2M (black) plotted with Sint-2000 (blue) and PISO-1500 (red) models. Grey bars indicate known reversals. Top: 0–1 Ma. Bottom: 1–2 Ma.

Table 2. Comparison of model statistics.

Model	μ_{2M}	σ_{2M}	μ_b	σ_b	μ_m	σ_m
PLS spline	6.0	1.4	7.2	1.2	5.3	1.0
PADM2Mp	5.3	1.7	6.2	1.5	4.8	1.5
PADM2M	5.3	1.5	6.2	1.2	4.8	1.4
Sint-2000	6.2	2.0	7.6	1.7	5.3	1.6
PISO-1500	–	–	7.5	2.6	–	–

Notes: Mean (μ) and one standard deviation (σ) of the four axial dipole models discussed in text and the Penalized Least Squares fit (PLS Spline) to absolute palaeointensities used in the construction of PADM2M over three age ranges. Subscripts 2M, b and m represent age ranges of: 0–2 Ma, 0–0.78 Ma (the Brunhes chron) and 0.78–2 Ma, respectively.

field strength of $5.3 \times 10^{22} \text{ Am}^2$ for the last 2 Ma and a standard deviation of $1.5 \times 10^{22} \text{ Am}^2$. There is a difference in mean between the Brunhes and older portion of both the PADM2M and PADM2Mp of $1.4 \times 10^{22} \text{ Am}^2$ (see Table 2). For PADM2M (evaluated every 1 ka), the average Brunhes model and average upper and lower model bounds are 6.2, 5.9 and $6.5 \times 10^{22} \text{ Am}^2$; for the 0.78–2 Ma Matuyama segment, these numbers are 4.8, 4.5 and

$5.4 \times 10^{22} \text{ Am}^2$. The non-overlapping bounds show that the means of the Brunhes and Matuyama chrons are distinctly different. PADM2Mp shows similar non-overlapping bounds. This result is consistent with the conclusions of Valet *et al.* (2005) for Sint-2000, but with a smaller difference in mean PADM for the two chrons (1.4 versus $2.3 \times 10^{22} \text{ Am}^2$). For PISO-1500 the difference in chron means is $0.7 \times 10^{22} \text{ Am}^2$, and is considered statistically insignificant. For perspective, Table 2 also lists means over these time ranges for the preliminary PLS low resolution model fit, the first step of our PML algorithm. This preliminary estimate is made only from API data and does not include the ML estimation, hence the overall higher mean values. Yet the PLS spline also shows a substantial difference in chron means (of $1.9 \times 10^{22} \text{ Am}^2$). The difference in means seen in PADM2M and Sint-2000 is not confined to the RPI data sets. This is important because it rules out possible VRM contamination of RPI records as a source of differences in the Brunhes and Matuyama chron means.

The lowest value of PADM2M is $1.08 \times 10^{22} \text{ Am}^2$ and occurs at 1.208 Ma (the Cobb Mountain Excursion), with other reversals having similar lows. The highest PADM2M of $9.7 \times 10^{22} \text{ Am}^2$

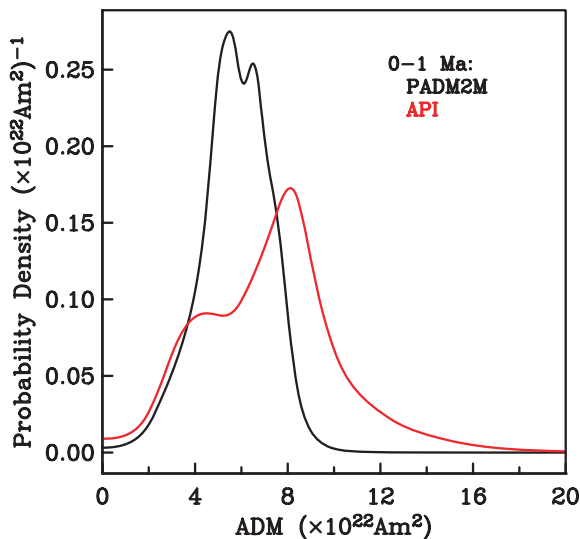


Figure 10. 0–1 Ma axial dipole moment distribution for PADM2M (black), along with 0–1 Ma axial dipole moment distribution from API data found in Ziegler *et al.* (2008) (red).

occurs at 2 ka; the highest value outside the last few thousand years is slightly lower at $9.3 \times 10^{22} \text{ Am}^2$ and occurs at 0.657 Ma. Many of the highest values of 0–2 Ma API derived VADMs in the PINT08 database are from 2 to 3 ka as well, indicating that the intensity peak of 2–3 ka may be the high point of the last 2 Myr. Some individual archaeointensities also show a very high field at this age (see e.g. Ben-Yosef *et al.* (2009)). However, the first few thousand years of our model are constrained primarily by API data, which can capture the true high frequency variation of the field in this time interval better than the inherently smoothed RPI records that constrain most of the model. This limitation of low sedimentation rate RPI data makes it unlikely that they can fully recover the true magnitude of older peaks.

Fig. 10 compares the distribution of the PADM2M model with the API distribution from Ziegler *et al.* (2008) for 0–1 Ma. As expected, the model distribution shows a smaller variance, because high frequency field variations are averaged out by the sedimentary processes and lost in model fitting. In the case of PADM2M, resolution is on the order of 10 kyr. The model pdf shows a variation of the slightly bimodal distribution seen in the API distribution, supporting the conclusions in Ziegler *et al.* (2008) that this feature is likely an accurate representation of the true distribution and temporal variations of 0–1 Ma intensities rather than an artefact generated by subsets of poor quality data.

5.3 Power spectrum

We calculate the power spectrum of PADM2M, both to look for any signals associated with orbital frequencies and to compare it with the palaeomagnetic power spectrum Constable & Johnson (2005) constructed from several separate field models and sediment records. The PADM2M spectrum is calculated using the same multi-taper spectral estimation techniques described in Constable & Johnson (2005).

Plotting the PADM2M spectrum along with the palaeomagnetic power spectrum (Fig. 11), we see that the PADM2M spectrum lies on top of portions corresponding to moderate resolution sediment records. At frequencies higher than 10^2 Myr^{-1} , the slope of the spectrum is proportional to f^{-8} which reflects the power spec-

trum associated with the effective filter of the smoothing spline regularization (Constable & Parker 1991) and is not characteristic of the data. As mentioned in Section 4, we have intentionally chosen an amount of regularization which filters out these high frequencies, considering them unreliably estimated by the currently available data. We calculate and plot the power spectra of Sint-2000 and PISO-1500 for comparison. Sint-2000 has a power spectrum similar to PADM2M, whereas PISO-1500 has additional energy at higher frequencies because it is constructed from higher resolution, geomagnetically tuned sediment records and agrees with the portion of the palaeomagnetic power spectrum constructed from high resolution sediment records.

Some authors have seen a correlation between orbital cycles (i.e. eccentricity, obliquity and precession) and RPI records (e.g. Channell *et al.* 1998; Channell & Kleiven 2000; Yamazaki & Kanamatsu 2007). The PADM2M spectrum has no peaks in power at orbital cycle frequencies (e.g. periods of 23, 41 or 100 kyr), or at any others. Therefore, our model, in agreement with other VADM models like PISO-1500 (Channell *et al.* 2009), shows no obvious connection between orbital cycles and geomagnetic field behaviour.

5.4 Anomalous data

In Section 4, we found that some records strongly disagreed with the PADM2M model. From visual assessment, most of these anomalous records seemed similar to the model, except that the ages of peaks and lows would often be offset from those of the model. This indicates that misfit has more to do with timing errors than errors in palaeointensity measurements. Some rock magnetic information from sediments in regions producing the anomalous RPI data suggest the data are possibly affected by reduction diagenesis and record a lag between the age of the sediments and the age of remanent magnetization acquisition (e.g. Stoner *et al.* 2003; Rowan *et al.* 2009). Because our ML method attributes the noise to intensity uncertainties, and explicitly uses the pdf associated with the noise/residuals in the estimation procedure, it was inappropriate to use these data with this method. However, efforts to incorporate timing uncertainties into future methods might allow for the use of these records.

Six of the rejected RPI series are categorized as LR and four are YR (see Table 2). Of the six LR, four are from the southern hemisphere—whereas eight of the total 34 LR are southern hemisphere. This disproportionate misfit of southern hemisphere records may indicate that there are real regional differences in palaeointensity signals, in addition to or instead of only timing errors. An investigation of this is beyond the scope of this paper, but suggests that it might be useful to make separate regional models using our PML method and compare the results.

6 CONCLUSIONS

We have developed a method for efficiently generating PADM models from a joint set of API data and many RPI time-series. The use of PML fitting criteria minimizes the influence of outliers and avoids bias in the fit due to the asymmetric noise associated with palaeomagnetic data. We generate PADM2M, a time-varying, 2 Myr model with 5–10 kyr resolution, and confirm that it often agrees both with the data and with other recent axial dipole moment models, with some notable differences discussed in Section 5.

We find that the Brunhes chron shows a mean about 20 per cent higher than that for the Matuyama, but note that our model does not cover the entire Matuyama chron. This result was seen in

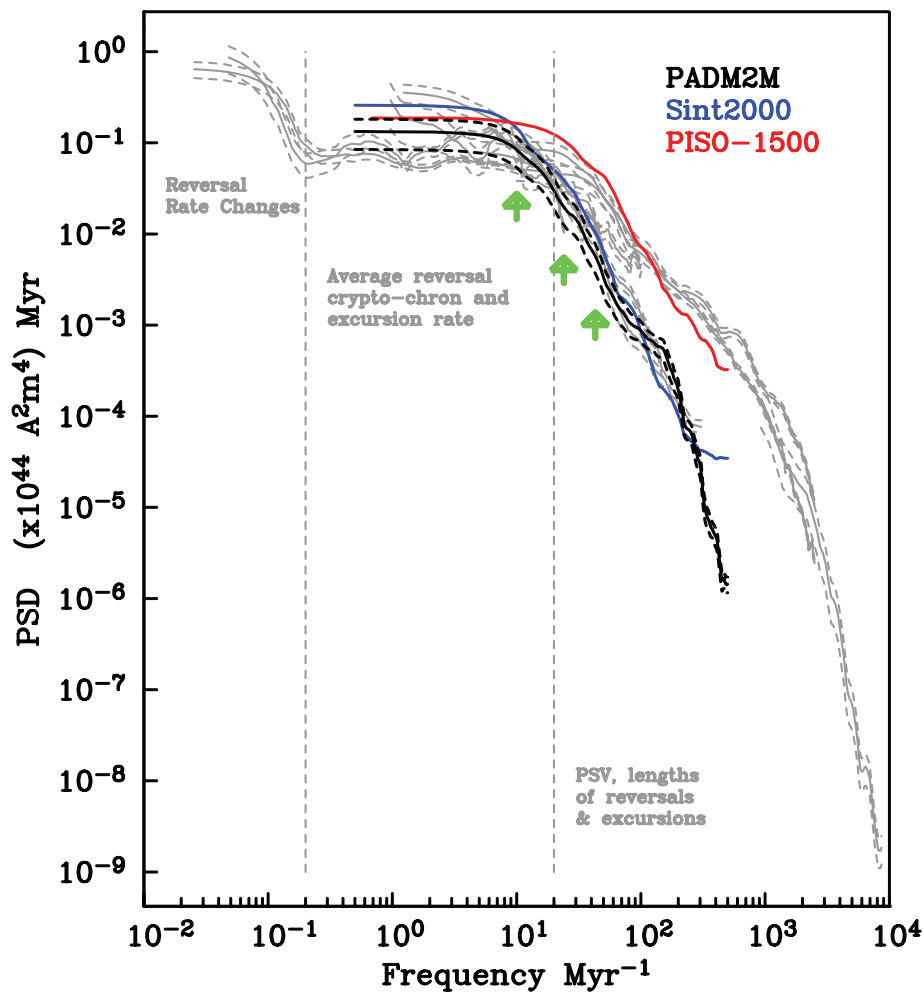


Figure 11. Power spectral density function of PADM2M (black), Sint-2000 (blue) and PISO-1500 (red) plotted on top of the composite palaeomagnetic power spectrum of Constable & Johnson (2005) (grey). Dashed lines represent $\pm 2\sigma$ bounds. Green arrows indicate frequencies of 23, 41 and 100 kyr, corresponding to orbital periods.

our PADM2M model, in a nine record version (PADM2Mp) made from only very long RPI records, which have significant amounts of data both before and after the reversal, and in an interim model based only on API data so we are confident the observation is not a result of our scaling or modelling procedures. Field strength models alone cannot resolve whether this reflects any difference in geodynamo processes during the two chrons or whether it is simply an observation of non-stationarity of the field over 2 Myr intervals.

The power spectrum of PADM2M shows no extra power at orbital frequencies, indicating that the field strength has no strong correlation with orbital forcing. A comparison with the palaeomagnetic power spectrum of Constable & Johnson (2005) shows that as expected, some high frequency energy is lost through the process of finding a best fitting model to a highly variable set of data.

Our modelling efforts were able to incorporate both API data and RPI data sets with a range of lengths, sedimentation rates (and therefore, resolutions) and global locations. We examined quantitatively how well each data set fit with a resulting model and found a subset of records which fit poorly. Although we eliminated these records from our final model, we do not conclude that they are simply ‘bad’ data or unusable. Rather, this result points to the need to address timing uncertainties and more complicated geographic structure in future palaeomagnetic field models.

ACKNOWLEDGMENTS

We are grateful to Ivana Komunjer for code and helpful discussions regarding APD functions. Peter Spellucci provided the optimization subroutine donlp2 which was incorporated in the PML routine to calculate APD parameters. We thank Toshi Yamazaki and an anonymous reviewer for their constructive comments on the manuscript, which improved this paper. This work was supported under NSF grant EAR-0809709. CLJ acknowledges support from NSERC.

REFERENCES

- Amit, H. & Olson, P., 2006. Time-average and time-dependent parts of core flow, *Phys. Earth planet. Int.*, **155**(1–2), 120–139.
- Ben-Yosef, E., Tauxe, L., Levy, T.E., Shaar, R., Ron, H. & Najar, M., 2009. Geomagnetic intensity spike recorded in high resolution slag deposit in Southern Jordan, *Earth planet. Sci. Lett.*, **287**(3–4), 529–539.
- Biggin, A.J., Strik, G.H.M.A. & Langereis, C.G., 2009. The intensity of the geomagnetic field in the late-Archaeon: new measurements and an analysis of the updated IAGA palaeointensity database, *Earth Planets Space*, **61**(1), 9–22.
- Bloxham, J. & Jackson, A., 1992. Time-dependent mapping of the magnetic-field at the core-mantle boundary, *J. geophys. Res.*, **97**(B13), 19 537–19 563.
- Brachfeld, S. *et al.*, 2003. Holocene history of the Larsen-A Ice Shelf constrained by geomagnetic palaeointensity dating, *Geology*, **31**(9), 749–752.

- Cande, S. & Kent, D., 1995. Revised calibration of the geomagnetic polarity timescale for the late Cretaceous and Cenozoic, *J. geophys. Res.*, **100**(B4), 6093–6095.
- Carcaillat, J.T., Thouveny, N. & Bourles, D.L., 2003. Geomagnetic moment instability between 0.6 and 1.3 Ma from cosmoclock evidence, *Geophys. Res. Lett.*, **30**(15), 1792, doi:10.1029/2003GL017550.
- Channell, J., Stoner, J., Hodell, D. & Charles, C., 2000. Geomagnetic paleointensity for the last 100 kyr from the sub-antarctic South Atlantic: a tool for inter-hemispheric correlation, *Earth planet. Sci. Lett.*, **175**, 145–160.
- Channell, J.E.T., 1999. Geomagnetic paleointensity and directional secular variation at Ocean Drilling Program (ODP) Site 984 (Bjorn Drift) since 500 ka: comparisons with ODP Site 983 (Gardar Drift), *J. geophys. Res.*, **104**(B10), 22 937–22 951.
- Channell, J.E.T. & Kleiven, H.F., 2000. Geomagnetic palaeointensities and astrochronological ages for the Matuyama-Brunhes boundary and the boundaries of the Jaramillo Subchron: palaeomagnetic and oxygen isotope records from ODP Site 983, *Phil. Trans. R. Soc. Lond., A.*, **358**(1768), 1027–1047.
- Channell, J.E.T., Hodell, D.A. & Lehman, B., 1997. Relative geomagnetic paleointensity and ^{18}O at ODP Site 983 (Gardar Drift, North Atlantic) since 350 ka, *Earth planet. Sci. Lett.*, **153**, 103–118.
- Channell, J.E.T., Hodell, D.A., McManus, J. & Lehman, B., 1998. Orbital modulation of the Earth's magnetic field intensity, *Nature*, **394**(6692), 464–468.
- Channell, J.E.T., Mazaud, A., Sullivan, P., Turner, S. & Raymo, M.E., 2002. Geomagnetic excursions and paleointensities in the Matuyama Chron at Ocean Drilling Program Sites 983 and 984 (Iceland Basin), *J. geophys. Res.*, **107**(B6), 2114, doi:10.1029/2001JB000491.
- Channell, J.E.T., Curtis, J.H. & Flower, B.P., 2004. The Matuyama-Brunhes boundary interval (500–900 ka) in North Atlantic drift sediments, *Geophys. J. Int.*, **158**(2), 489–505.
- Channell, J.E.T., Xuan, C. & Hodell, D.A., 2009. Stacking paleointensity and oxygen isotope data for the last 1.5 Myr (PISO-1500), *Earth planet. Sci. Lett.*, **283**(1–4), 14–23.
- Clement, B. & Kent, D., 1991. A southern-hemisphere record of the Matuyama-Brunhes polarity reversal, *Geophys. Res. Lett.*, **18**(1), 81–84.
- Clement, B.M. & Kent, D.V., 1986. Short polarity intervals within the Matuyama: transitional field records from hydraulic piston cored sediments from the North Atlantic, *Earth planet. Sci. Lett.*, **81**, 253–264.
- Constable, C., 1988. Parameter-estimation in non-gaussian noise, *Geophys. J.*, **94**(1), 131–142.
- Constable, C. & Parker, R., 1988. Smoothing, splines, and smoothing splines—their application in geomagnetism, *J. Comput. Phys.*, **78**(2), 493–508.
- Constable, C. & Parker, R., 1991. Deconvolution of long-core paleomagnetic measurements—spline therapy for the linear problem, *Geophys. J. Int.*, **104**(3), 453–468.
- Constable, C. & Johnson, C., 2005. A paleomagnetic power spectrum, *Phys. Earth planet. Int.*, **153**(1–3, Special Issue SI), 61–73.
- Constable, S.C., Parker, R.L. & Constable, C.G., 1987. Occam's Inversion: a practical inversion method for generating smooth models from EM sounding data, *Geophysics*, **52**, 289–300, doi:10.1190/1.1442303.
- Dinares-Turell, J., Sagnotti, L. & Roberts, A.P., 2002. Relative geomagnetic paleointensity from the Jaramillo Subchron to the Matuyama/Brunhes boundary as recorded in a Mediterranean piston core, *Earth planet. Sci. Lett.*, **194**(3–4), 327–341.
- Donadini, F., Korte, M. & Constable, C.G., 2009. Geomagnetic field for 0–3 ka: 1. New data sets for global modeling, *Geochem. Geophys. Geosyst.*, **10**, Q06007, doi:10.1029/2008GC002295.
- Driscoll, P. & Olson, P., 2009. Polarity reversals in geodynamo models with core evolution, *Earth planet. Sci. Lett.*, **282**(1–4), 24–33.
- Dumberry, M. & Finlay, C.C., 2007. Eastward and westward drift of the Earth's magnetic field for the last three millennia, *Earth planet. Sci. Lett.*, **254**(1–2), 146–157.
- Guyodo, Y. & Valet, J.P., 2006. A comparison of relative paleointensity records of the Matuyama Chron for the period 0.75–1.25 Ma, *Phys. Earth planet. Int.*, **156**, 205–212.
- Guyodo, Y., Richter, C. & Valet, J.P., 1999. Paleointensity record from Pleistocene sediments off the California Margin, *J. Geophys.*, **104**, 22 953–22 965.
- Guyodo, Y., Acton, G.D., Brachfeld, S. & Channell, J.E.T., 2001. A sedimentary paleomagnetic record of the Matuyama chron from the Western Antarctic margin (ODP Site 1101), *Earth planet. Sci. Lett.*, **191**(1–2), 61–74.
- Haag, M., 2000. Reliability of relative palaeointensities of a sediment core with climatically-triggered strong magnetisation changes, *Earth planet. Sci. Lett.*, **180**(1–2), 49–59.
- Hartl, P. & Tauxe, L., 1996. A precursor to the Matuyama/Brunhes transition-field instability as recorded in pelagic sediments, *Earth planet. Sci. Lett.*, **138**, 121–135.
- Hayashida, A., Verosub, K.L., Heider, F. & Leonhardt, R., 1999. Magnetostratigraphy and relative palaeointensity of late Neogene sediments at ODP Leg 167 Site 1010 off Baja California, *Geophys. J. Int.*, **139**(3), 829–840.
- Hornig, C.S., Roberts, A.P. & Liang, W.T., 2003. A 2.14-Myr astronomically tuned record of relative geomagnetic paleointensity from the western Philippine Sea, *J. geophys. Res.*, **108**(B1), 2059, doi:10.1029/2001JB001698.
- Jackson, A., Jonkers, A. & Walker, M., 2000. Four centuries of geomagnetic secular variation from historical records, *Phil. Trans. R. Soc. Lond.*, **358**, 957–990.
- Johnson, C. & McFadden, P., 2007. Time-averaged field and paleosecular variation, in *Geomagnetism*, Vol. 5 of Treatise on Geophysics, pp. 417–453, eds Kono, M., and Schubert, G., Elsevier, Amsterdam.
- Johnson, C.L. et al., 2008. Recent investigations of the 0–5 Ma geomagnetic field recorded by lava flows, *Geochem. Geophys. Geosyst.*, **9**, Q04032, doi:10.1029/2007GC001696.
- Kent, D.V. & Opdyke, N.D., 1977. Paleomagnetic field intensity variation recorded in a Brunhes epoch deep-sea sediment core, *Nature*, **266**, 156–159.
- Kent, D.V. & Schneider, D.A., 1995. Correlation of paleointensity variation records in the Brunhes/Matuyama polarity transition interval, *Earth planet. Sci. Lett.*, **129**, 135–144.
- Kissel, C., Laj, C., Labeyrie, L., Dokken, T., Voelker, A. & Blamart, D., 1999. Rapid climatic variations during marine isotopic stage 3: magnetic analysis of sediments from Nordic Seas and North Atlantic, *Earth planet. Sci. Lett.*, **171**(3), 489–502.
- Kok, Y.S. & Tauxe, L., 1999. A relative geomagnetic paleointensity stack from Ontong-Java Plateau sediments for the Matuyama, *J. geophys. Res.*, **104**(B11), 25 401–25 413.
- Komunjer, I., 2007. Asymmetric power distribution: theory and applications to risk measurement, *J. appl. Econometrics*, **22**(5), 891–921.
- Korte, M. & Constable, C., 2005. The geomagnetic dipole moment over the last 7000 years—new results from a global model, *Earth planet. Sci. Lett.*, **236**(1–2), 348–358.
- Korte, M., Donadini, F. & Constable, C.G., 2009. Geomagnetic field for 0–3 ka: 2. A new series of time-varying global models, *Geochem. Geophys. Geosyst.*, **10**, Q06008, doi:10.1029/2008GC002297.
- Laj, C., Kissel, C. & Lefevre, I., 1996. Relative geomagnetic field intensity and reversals from Upper Miocene sections in Crete, *Earth planet. Sci. Lett.*, **141**(1–4), 67–78.
- Laj, C., Kissel, C., Mazaud, A., Channell, J. & Beer, J., 2000. North Atlantic palaeointensity stack since 75 ka (NAPIS-75) and the duration of the Laschamp event, *Phil. Trans. R. Soc. Lond.*, **358**, 1009–1025.
- Lawrence, K.P., Tauxe, L., Staudigel, H., Constable, C.G., Koppers, A., McIntosh, W. & Johnson, C.L., 2009. Paleomagnetic field properties at high southern latitude, *Geochem. Geophys. Geosyst.*, **10**, Q01005, doi:10.1029/2008GC002072.
- Lehman, B., Laj, C., Kissel, C., Mazaud, A., Paterne, M. & Labeyrie, L., 1996. Relative changes of the geomagnetic field intensity during the last 280 kyr from piston cores in the Açores area, *Phys. Earth planet. Inter.*, **93**, 269–284.
- Leonhardt, R., Heider, F. & Hayashida, A., 1999. Relative geomagnetic field intensity across the Jaramillo subchron in sediments from the California margin: ODP Leg 167, *J. geophys. Res.*, **104**, 29 133–29 146.

- Lisiecki, L. & Lisiecki, P., 2002. Application of dynamic programming to the correlation of paleoclimate records, *Paleoceanography*, **17**(4), 1049, doi:10.1029/2001PA000733.
- Love, J. & Constable, C., 2003. Gaussian statistics for palaeomagnetic vectors, *Geophys. J. Int.*, **152**(3), 515–565.
- Maus, S. *et al.*, 2005. The 10th generation international geomagnetic reference field, *Phys. Earth planet. Int.*, **151**, 320–322.
- McFadden, P. & McElhinny, M., 1982. Variations in the geomagnetic dipole: statistical analysis of VDMs for the past 5 million years, *J. Geomagn. Geoelectr.*, **34**(3), 163–189.
- McFadden, P. & Merrill, R., 1997. Sawtooth paleointensity and reversals of the geomagnetic field, *Phys. Earth planet. Int.*, **103**(3–4), 247–252.
- McMillan, D., Constable, C. & Parker, R., 2002. Limitations on stratigraphic analyses due to incomplete age control and their relevance to sedimentary paleomagnetism, *Earth planet. Sci. Lett.*, **201**(3–4), 509–523.
- Meynadier, L., Valet, J.P., Weeks, R., Shackleton, N.J. & Hagee, V.L., 1992. Relative geomagnetic intensity of the field during the last 140 ka, *Earth planet. Sci. Lett.*, **114**, 39–57.
- Meynadier, L., Valet, J.P., Bassinot, F., Shackleton, N.J. & Guyodo, Y., 1994. Asymmetrical saw-tooth pattern of the geomagnetic field intensity from equatorial sediments in the Pacific and Indian Oceans, *Earth planet. Sci. Lett.*, **126**, 109–127.
- Nowaczyk, N.R. & Frederichs, T.W., 1999. Geomagnetic events and relative palaeointensity variations during the past 300 ka as recorded in Kolbeinsey Ridge sediments, Iceland Sea: indication for a strongly variable geomagnetic field, *Int. J. Earth Sci.*, **88**(1), 116–131.
- Oda, H., Nakamura, K., Ikehara, K., Nakano, T., Nishimura, M. & Khlystov, O., 2002. Paleomagnetic record from Academician Ridge, Lake Baikal: a reversal excursion at the base of marine oxygen isotope stage 6, *Earth planet. Sci. Lett.*, **202**(1), 117–132.
- Okada, M., 1995. Detailed variation of geomagnetic field intensity during the late Pleistocene at Site 882, *Proc. Ocean Drill. Program, Sci. Results*, **145**, 469–474.
- Parker, R.L., 1994. *Geophysical Inverse Theory*, Princeton University Press, Princeton, NJ.
- Peck, J., King, J., Colman, S. & Kravchinsky, V., 1996. An 84-kyr paleomagnetic record from the sediments of Lake Baikal, Siberia, *J. geophys. Res.*, **101**, 11 365–11 385.
- Press, W.H., Teukolsky, S.A., Vetterling, W.T. & Flannery, B.P., 1986. *Numerical Recipes in Fortran 77: The Art of Scientific Computing*, Cambridge University Press, New York, NY.
- Rice, J.A., 1995. *Mathematical Statistics and Data Analysis*, 2nd edn, Duxbury Press, Belmont, CA.
- Roberts, A., Lehman, B., Weeks, R., Verosub, K. & Laj, C., 1997. Relative paleointensity of the geomagnetic field over the last 200,000 years from ODP Sites 883 and 884, North Pacific Ocean, *Earth planet. Sci. Lett.*, **152**, 11–23.
- Roberts, A.P. & Winklhofer, M., 2004. Why are geomagnetic excursions not always recorded in sediments? Constraints from post-depositional remanent magnetization lock-in modelling, *Earth planet. Sci. Lett.*, **227**(3–4), 345–359.
- Rowan, C.J., Roberts, A.P. & Broadbent, T., 2009. Reductive diagenesis, magnetite dissolution, greigite growth and paleomagnetic smoothing in marine sediments: a new view, *Earth planet. Sci. Lett.*, **277**(1–2), 223–235.
- Sato, T. & Kobayashi, K., 1989. Long-period secular variations of the Earth's magnetic field revealed by Pacific deep-sea sediment cores, *J. Geomagn. Geoelectr.*, **41**, 147–159.
- Sato, T., Kikuchi, H., Nakashizuka, M. & Okada, M., 1998. Quaternary geomagnetic field intensity: constant periodicity or variable period?, *Geophys. Res. Lett.*, **25**, 2221–2224.
- Schneider, D. & Mello, G., 1996. A high-resolution marine sedimentary record of geomagnetic intensity during the Brunhes chron, *Earth planet. Sci. Lett.*, **144**, 297–314.
- Schneider, D.A., 1993. An estimate of Late Pleistocene geomagnetic intensity variation From Sulu Sea sediments, *Earth planet. Sci. Lett.*, **120**(3–4), 301–310.
- Schneider, D.A., Kent, D.V. & Mello, G.A., 1992. A detailed chronology of the Australasian impact event, the Brunhes-Matuyama geomagnetic polarity reversal and global climate change, *Earth planet. Sci. Lett.*, **111**, 395–405.
- Schwartz, M., Lund, S.P. & Johnson, T.C., 1996. Environmental factors as complicating influences in the recovery of quantitative geomagnetic-field paleointensity estimates from sediments, *Geophys. Res. Lett.*, **23**, 2693–2696.
- Singer, B.S., Hoffman, K.A., Schnepf, E. & Guillou, H., 2008. Multiple Brunhes Chron excursions recorded in the West Eifel (Germany) volcanics: support for long-held mantle control over the non-axial dipole field, *Phys. Earth planet. Int.*, **169**(1–4, Special Issue SI), 28–40.
- Stoner, J., Channell, J. & Hillaire-Marcel, C., 1998. A 200 ka geomagnetic chronostratigraphy for the Labrador Sea: indirect correlation of the sediment record to SPECMAP, *Earth planet. Sci. Lett.*, **159**(3–4), 165–181.
- Stoner, J., Channell, J., Hillaire-Marcel, C. & Kissel, C., 2000. Geomagnetic paleointensity and environmental record from Labrador sea core md95-2024: global marine sediment and ice core chronostratigraphy for the last 110 kyr, *Earth planet. Sci. Lett.*, **5626**, 1–17.
- Stoner, J., Laj, C., Channell, J. & Kissel, C., 2002. South Atlantic and North Atlantic geomagnetic paleointensity stacks (0–80 ka): implications for inter-hemispheric correlation, *Quat. Sci. Rev.*, **21**(10), 1141–1151.
- Stoner, J.S., Channell, J.E.T., Hodell, D.A. & Charles, C.D., 2003. A ~580 kyr paleomagnetic record from the sub-Antarctic South Atlantic (Ocean Drilling Program Site 1089), *J. geophys. Res.*, **108**(B5), 2244, doi:10.1029/2001JB001390.
- Stott, L., Poulsen, C., Lund, S. & Thunell, R., 2002. Super ENSO and global climate oscillations at millennial time scales, *Science*, **297**, 222–226.
- Tauxe, L. & Shackleton, N.J., 1994. Relative paleointensity records from the Ontong-java Plateau, *Geophys. J. Int.*, **117**, 769–782.
- Tauxe, L. & Wu, G., 1990. Normalized remanence in sediments of the Western Equatorial Pacific: relative paleointensity of the geomagnetic field?, *J. geophys. Res.*, **95**(B8), 12 337–12 350.
- Tauxe, L. & Yamazaki, T., 2007. Paleointensities, in *Geomagnetism*, Vol. 5 of Treatise on Geophysics, pp. 509–563, eds Kono, M. and Schubert, G., Elsevier, Amsterdam.
- Thellier, E. & Thellier, O., 1959. Sur l'intensité du champ magnétique terrestre dans le passé historique et géologique, *Ann. Geophys.*, **15**, 258–378.
- Thouveny, N. *et al.*, 1994. Climate variations in Europe over the past 140-kyr deduced from rock magnetism, *Nature*, **371**(6497), 503–506.
- Thouveny, N., Carcaillet, J., Moreno, E., Leduc, G. & Nerini, D., 2004. Geomagnetic moment variation and paleomagnetic excursions since 400 kyr BP: a stacked record from sedimentary sequences of the Portuguese margin, Pt 1, *Earth planet. Sci. Lett.*, **219**(3–4), 377–396.
- Tric, E., Valet, J.P., Tucholka, P., Paterne, M., LaBeyrie, L., Guichard, F., Tauxe, L. & Fontugne, M., 1992. Paleointensity of the geomagnetic field during the last 80 000 years, *J. geophys. Res.*, **97**, 9337–9351.
- Valet, J., 2003. Time variations in geomagnetic intensity, *Rev. Geophys.*, **41**(1), 1004, doi:10.1029/2001RG000104.
- Valet, J. & Meynadier, L., 1993. Geomagnetic-field intensity and reversals during the past 4 million years, *Nature*, **366**(6452), 234–238.
- Valet, J., Meynadier, L. & Guyodo, Y., 2005. Geomagnetic dipole strength and reversal rate over the past two million years, *Nature*, **435**(7043), 802–805.
- Valet, J.P., Meynadier, L., Bassinot, F.C. & Garnier, F., 1994. Relative paleointensity across the last geomagnetic reversal from sediments of the Atlantic, Indian and Pacific Oceans, *Geophys. Res. Lett.*, **21**, 485–488.
- Valet, J.P., Tauxe, L. & Clement, B.M., 1989. Equatorial and mid-latitude records of the last geomagnetic reversal from the Atlantic Ocean, *Earth planet. Sci. Lett.*, **94**, 371–384.
- Wardinski, I. & Korte, M., 2008. The evolution of the core-surface flow over the last seven thousands years, *J. geophys. Res.*, **113**(B5), doi:10.1029/2007JB005024
- Weeks, R.J., Laj, C., Endignoux, L., Mazaud, A., Labeyrie, L., Roberts, A.P., Kissel, C. & Blanchard, E., 1995. Normalised natural remanent magnetisation intensity during the last 240 000 years in piston cores from the central North Atlantic Ocean: geomagnetic field intensity or environmental signal?, *Phys. Earth planet. Inter.*, **87**, 213–229.

Williams, T., Thouveny, N. & Creer, K.M., 1998. A normalised intensity record from Lac du Bouchet: geomagnetic palaeointensity for the last 300 kyr?, *Earth planet. Sci. Lett.*, **156**(1–2), 33–46.

Wilson, R., 1970. Permanent aspects of the Earth's non-dipole magnetic field over upper Tertiary times, *Geophys. J. R. astr. Soc.*, **19**(4), 417–439.

Yamazaki, T., 1999. Relative paleointensity of the geomagnetic field during Brunhes Chron recorded in North Pacific deep-sea sediment cores: orbital influence?, *Earth planet. Sci. Lett.*, **169**(1–2), 23–35.

Yamazaki, T. & Ioka, N., 1994. Long-term secular variation of the geomagnetic field during the last 200 kyr recorded in sediment cores from the western equatorial Pacific, *Earth planet. Sci. Lett.*, **128**, 527–544.

Yamazaki, T., Ioka, N. & Eguchi, N., 1995. Relative paleointensity of the geomagnetic field during the Brunhes Chron, *Earth planet. Sci. Lett.*, **136**, 525–540.

Yamazaki, T. & Kanamatsu, T., 2007. A relative paleointensity record of the geomagnetic field since 1.6 Ma from the North Pacific, *Earth Planets Space*, **59**(7), 785–794.

Yamazaki, T. & Oda, H., 2005. A geomagnetic paleointensity stack between 0.8 and 3.0 Ma from equatorial Pacific sediment cores, *Geochem. Geophys. Geosyst.*, **6**, Q11H20, doi: 10.2029/2005GC001001.

Ziegler, L.B., Constable, C.G. & Johnson, C.L., 2008. Testing the robustness and limitations of 0–1 Ma absolute paleointensity data, *Phys. Earth planet. Int.*, **170**(1–2), 34–45.

APPENDIX A: BIAS DUE TO NOISE IN ESTIMATING AXIAL DIPOLE MOMENT FROM VADM DATA

Intensity data are converted by a linear transformation to VADM data through the GAD field assumption, with non-axial-dipole (NAD) intensity contributions, measurement and recording error manifesting as noise in the VADM data. This noise is often implicitly assumed to be Gaussian—or at least symmetric—with a mean of zero. In palaeomagnetic studies VADM noise is generally treated as being zero-mean Gaussian so that on average, VADM is thought to represent the true axial dipole moment. We show below that the true PADM is non-linearly related to field intensity. Because of this non-linearity, VADMs produce a biased estimate of axial dipole moment.

We derive here the relationship between field intensity ($|B(t)|$) and axial dipole strength (g_1^0), including a consideration of NAD and other implicit noise. At any given location we express the measured squared field strength as

$$B^2(r, \theta, \phi, t) = B^2(t) = [B_r(t)^2 + B_\theta(t)^2 + B_\phi(t)^2] \quad (\text{A1})$$

$$= [k_r g_1^0(t) + R]^2 + [k_\theta g_1^0(t) + T]^2 + (H)^2, \quad (\text{A2})$$

where $k_r = 2 \cos \theta$ and $k_\theta = \sin \theta$ and R, T, H are independent random variables which express NAD contributions to the field strength. They might be Gaussian, but relaxing that restriction allows for a more flexible approach to noise contributions. For now, we can suppose that $E[R] = E[T] = E[H] = 0$ and has no time variation (implying NAD vector field contributions average to zero).

Taking (A2) and expanding the RHS we get a quadratic equation that can be solved for $g_1^0(t)$, namely

$$(k_r^2 + k_\theta^2)[g_1^0(t)]^2 + 2(k_r R + k_\theta T)g_1^0(t) + R^2 + T^2 + H^2 - B^2(t) = 0. \quad (\text{A3})$$

Solving for $g_1^0(t)$ we find

$$g_1^0(t) = \pm \frac{B(t)}{(k_r^2 + k_\theta^2)^{1/2}} \left[1 - \frac{(R^2 + T^2 + H^2)}{[B(t)]^2} + \frac{k_r R + k_\theta T}{[B(t)]^2 (k_r^2 + k_\theta^2)} \right]^{1/2} - \frac{k_r R + k_\theta T}{(k_r^2 + k_\theta^2)} \quad (\text{A4})$$

and invoking the binomial expansion

$$g_1^0(t) \approx \pm \frac{B(t)}{(k_r^2 + k_\theta^2)^{1/2}} \left[1 - \frac{(R^2 + T^2 + H^2)}{2[B(t)]^2} + \frac{k_r R + k_\theta T}{2[B(t)]^2 (k_r^2 + k_\theta^2)} + \dots \right] - \frac{k_r R + k_\theta T}{(k_r^2 + k_\theta^2)}. \quad (\text{A5})$$

Transforming the axial dipole intensity, $g_1^0(t)$, into axial dipole moment is just a matter of multiplicative constants

$$\text{PADM}(t) = v(t) = \frac{4\pi r^3}{\mu_0} g_1^0(t) \quad (\text{A6})$$

with Earth average radius $r = 6371$ km and $\mu_0 = 4\pi \times 10^{-7}$ H m⁻¹. Applying this to eq. (A5) and noting that $(k_r^2 + k_\theta^2)^{1/2} = (1 + 3 \cos^2 \theta)^{1/2}$ gives the relationship between PADM and field intensity

$$v(t) \approx \pm \frac{4\pi r^3}{\mu_0 (1 + 3 \cos^2 \theta)^{1/2}} \left[B(t) - \frac{(R^2 + T^2 + H^2)}{2[B(t)]} + \frac{k_r R + k_\theta T}{2[B(t)](1 + 3 \cos^2 \theta)} + \dots \right] - \frac{4\pi r^3}{\mu_0} \frac{k_r R + k_\theta T}{(1 + 3 \cos^2 \theta)}. \quad (\text{A7})$$

The usual palaeomagnetic VADM [$V(t)$] is

$$V(t) = \frac{4\pi r^3}{\mu_0 (1 + 3 \cos^2 \theta)^{1/2}} B(t)$$

which is in fact the first (and largest) term on the RHS of the equation for PADM (A7). However, it takes no account of the additional RHS terms. If R, T and H are Gaussian random variables with zero means, the last term would be zero on average but the other terms would not. In practice, R, T and H are not known, but one can restate the relationship between PADM and VADM as

$$V(t) = v(t) + b,$$

where b is a bias term, which is a random variable of ‘noise’ which has a non-zero mean and an unknown (but certainly non-Gaussian) distribution function.

APPENDIX B: PML INVERSION

The PML algorithm follows the outline given in Section 3.5 and presented in the flowchart of Fig. 7. In Section B1, we outline how the PML method would be applied to a single time-series of API data with a common noise distribution, then in Section B2 discuss additional complexity associated with incorporating and calibrating heterogenous sediment records of variable resolution.

B1 PML for a single (Absolute) VADM data series

In Step 1, we follow the algorithm of Constable & Parker (1988) to find $v_0(t)$, a penalized cubic B-spline model of PADM for a single (absolute) palaeointensity data series. The observations ($d_i, i = 1, \dots, n$) are represented as a linear combination of cubic B-spline basis functions $c_j(t_i)$ and a noise term (ϵ_i)

$$d_i = v(t_i) + \epsilon_i = \sum_{j=1}^p \beta_j c_j(t_i) + \epsilon_i, \tag{B1}$$

where β_j are the corresponding spline coefficients and are the initial model parameters we seek. In this first step, we do not yet have an estimate for the noise distribution so the objective functional minimized over $\hat{\beta}$ is

$$U(\hat{\beta}) = l_0(\hat{\beta}) + \Lambda R(\hat{\beta}) \tag{B2}$$

with $l_0(\hat{\beta})$ corresponding to the standard 2-norm misfit measure anticipated for a least squares fit. That is

$$l_0(\hat{\beta}) = \sum_{i=1}^n [d_i - v_0(t_i)]^2 = \sum_{i=1}^n \epsilon_i^2. \tag{B3}$$

The model roughness, $R(\hat{\beta})$, is given by the integrated squared second derivative of the resulting spline

$$R(\hat{\beta}) = \int_{t_i}^{t_n} \left[\partial_t^2 \sum_{j=1}^p \beta_j c_j(t) \right]^2 dt. \tag{B4}$$

The trade-off parameter Λ in eq. (B2) controls the balance between fitting the data and penalizing roughness in $v(t)$.

The usual ML method finds the parameter estimates which maximize the probability of getting the data that were actually observed using an appropriate pdf for the noise. The function to be maximized in this case, the likelihood function, $L(\hat{\beta})$, is the joint pdf, F , of the sample errors, which is in turn the product of the individual pdfs if the errors are independent, identically distributed

$$L(\hat{\beta}) = F(\epsilon, \hat{\beta}) = \prod_{i=1}^n f(\epsilon_i, \hat{\beta}). \tag{B5}$$

Step 2 is to make a first estimate of the noise distribution $f(\epsilon)$, using the residuals of the data from $v_0(t)$. For a given data set, we describe the statistical distribution of the residuals (ϵ_i) using an APD, whose pdf function is by definition

$$f(\epsilon_i) = \frac{\delta_{\alpha,\lambda}^{1/\lambda}}{\sigma \Gamma(1 + 1/\lambda)} \exp \left[-\frac{\delta_{\alpha,\lambda}}{\gamma(\epsilon_i)} \left| \frac{\epsilon_i - \mu}{\sigma} \right|^\lambda \right], \tag{B6}$$

where

$$\delta_{\alpha,\lambda} = \frac{2\alpha^\lambda(1-\alpha)^\lambda}{\alpha^\lambda + (1-\alpha)^\lambda} \tag{B7}$$

$$\begin{aligned} \gamma(\epsilon_i) &= \alpha^\lambda & \epsilon_i \leq \mu \\ &= (1-\alpha)^\lambda & \epsilon_i > \mu \end{aligned} \tag{B8}$$

and μ , σ , α and λ are the location, scale and two shape parameters, respectively. The shape parameter α has the range $0 < \alpha < 1$ and corresponds to asymmetry, where 0.5 means there is an equal amount of data on either side of the mode. The second shape parameter, λ , corresponds to tail shape and has the range $\lambda > 0$, though it is generally between 1 and 3 (see Table 1). High values of λ mean flatter-topped distributions, with $\lambda = 2$ (and $\alpha = 0.5$) corresponding to a symmetric Gaussian distribution (see Fig. 6). μ is unbounded and $\sigma > 0$.

We estimate the pdf parameters (μ , σ , α and λ) of the noise empirically from the residuals resulting from iterative PML fits

$$\epsilon_i^q = d_i - \sum_{j=1}^p \beta_j^{q-1} c_j(t_i), \tag{B9}$$

where q represents the q th iteration.

The maximum of likelihood and minimum of the negative log likelihood [$l(\hat{\beta})$] coincide, so we can rewrite the problem as

$$\max_{\hat{\beta}} L(\hat{\beta}) = \min_{\hat{\beta}} l(\hat{\beta}) = \min_{\hat{\beta}} \sum_{i=1}^n \rho(\epsilon_i), \tag{B10}$$

where $\rho(\epsilon) = -\ln[f(\epsilon, \hat{\beta})]$ and is termed the loss function.

Now, combining this with the APD description for f , we can define our condition to minimize as

$$\min_{\hat{\beta}} l(\hat{\beta}),$$

$$l(\hat{\beta}) = \sum_{i=1}^n -\ln[f(\epsilon_i, \hat{\beta})]$$

$$l(\hat{\beta}) = \sum_{i=1}^n -\ln \left[\frac{\delta^{1/\lambda}}{\sigma \Gamma(1 + \frac{1}{\lambda})} \right] + \frac{\delta}{\sigma^\lambda \gamma^\lambda} |\epsilon_i - \mu|^\lambda.$$

The minimum is found where the derivatives with respect to the parameters, β_j , are zero—that is, $\nabla l(\beta) = 0$. Using eq. (B9), we get

$$\frac{\partial l}{\partial \beta_j} = \sum_{i=1}^n \frac{\lambda \delta c_j(t_i)}{\sigma^\lambda \gamma^\lambda} \left| d_i - \sum_{j=1}^p \beta_j c_j(t_i) - \mu \right|^{\lambda-2} \left[d_i - \sum_{j=1}^p \beta_j c_j(t_i) - \mu \right] = 0. \quad (\text{B11})$$

Although this is non-linear it can be solved iteratively in the form of a weighted least squares problem (Constable 1988) by rewriting the above equation as

$$\frac{\partial l}{\partial \beta_j^q} = \sum_{i=1}^n w_i^q c_j(t_i) \left[\tilde{d}_i - \sum_{j=1}^p \beta_j^q c_j(t_i) \right] = 0 \quad (\text{B12})$$

$$w_i^q = \frac{\lambda \delta}{\sigma^\lambda \gamma^\lambda} \left| \tilde{d}_i - \sum_{j=1}^p \beta_j^{q-1} c_j(t_i) \right|^{\lambda-2} \quad (\text{B13})$$

$$\tilde{d}_i = d_i - \mu. \quad (\text{B14})$$

Note, the parameters $(\mu, \sigma, \alpha, \lambda)$ and δ are all derived from the $(q - 1)$ th iteration as well, though the superscripts have been left off in the above notation to avoid clutter. In matrix notation, we will express this as

$$\mathbf{C}^T \mathbf{W}_q \mathbf{C} \hat{\beta} = \mathbf{C}^T \mathbf{W}_q \mathbf{d}. \quad (\text{B15})$$

In (B15), \mathbf{C} is the design matrix of B-spline functions, \mathbf{d} the vector of observations, $\tilde{\mathbf{d}}_i, \hat{\beta}$ the model vector of coefficients β_j and \mathbf{W}_q is the $n \times n$ diagonal matrix of ‘weights’ calculated from residuals produced from the previous $(q - 1)$ th iteration. Successive iterations of $\hat{\beta}$ and weights are calculated until specified convergence criteria are reached. Recasting the solution of the non-linear ML problem as an iteratively reweighted least squares problem conveniently allows us to use the same algorithm as in Step 1 to recover a PML solution by adding the roughness penalty in eq. (B4). Eq. (B2) is thus directly updated to include the correct likelihood function $l_q(\beta)$ for the asymmetric noise distribution expected for the absolute VADM data.

$$U(\beta) = l_q(\hat{\beta}) + \Lambda R(\hat{\beta}). \quad (\text{B16})$$

We call the algorithm that solves eq. (B16) a PML inversion, because of the explicit trade-off between finding the ML solution and the penalty on roughness in the resulting model.

B2 Using RPI time-series in PML models

Section B1 has described fitting a PML model to a single data series of n absolute observations of VADM with a common noise distribution. In practice, we have both spot recordings of VADM from igneous samples, and several independent time-series of relative variations in VADM from sediment records. Multiple absolute data sets can be treated in the same way but with distinct noise pdfs where necessary. However, the incorporation of RPI data into our model requires appropriate choices for calibrating these data to absolute values and appropriate weightings of the contribution of series some of which are very densely sampled in time.

B2.1 Calibration of RPI data

The calibration of RPI observations is a simple scaling by a multiplicative factor to transform them to absolute values of VADM. Explicitly stated, for RPI we have $d_i = \zeta_k S_{k,i}$, where $S_{k,i}$ denotes the i th data point in the k th time-series and ζ_k is the scale value for the k th data set such that eq. (B1) becomes

$$\zeta_k S_{k,i} = \sum_{j=1}^p \beta_j c_j(t_{k,i}) + \zeta_k \epsilon_{k,i}. \quad (\text{B17})$$

We estimate scale values by finding a low resolution preliminary PADM model from the sparse API data. Using this model, we calculate the ratio of the model to the RPI time-series at each time, and use the median of this ratio as the scale estimate. There is a small bias-correction factor (Δ_k^{m-1}) needed for non-symmetric noise, where $\bar{\epsilon} \neq 0$. These scale estimates are then recalculated m times (usually two to three times) after an updated ML model is made from the absolute and scaled RPI data.

$$\zeta_k^m = \text{median} \left[\frac{\sum_{j=1}^p \beta_j^{m-1} c_j(t_i)}{S_{k,i} - \Delta_k^{m-1}} \right]. \tag{B18}$$

Note that Δ_k^{m-1} is the difference between the mean and the mode of a given set of ϵ_i normalized by the scale value, ζ_k^{m-1} (since ϵ_i are in essence scaled as the data are scaled).

B2.2 Temporal normalization

For RPI records, sediment type and accumulation rate directly control the resolution possible, since a finite thickness of sediment is required for palaeointensity analysis. Thus, each data point in the time-series provides a temporal average palaeointensity over hundreds or thousands of years. In addition, some studies of post-depositional remanent magnetization (pDRM) in sediments suggest that the process of remanent magnetization acquisition in sediments itself acts as a low-pass filter and may contribute to signal smoothing (e.g. Roberts & Winklhofer (2004)). For our goal of finding a global average of dipole moment, we want each time-series to contribute equally to the resulting model at any given time. We weight each sediment record so that it contributes equally over a given time range. There are two things to consider for this goal. First, high resolution records simply contain more data points over a given time range (sometimes an order of magnitude more), so we divide by the number of data (n_k) per age range (Δt) to reduce this influence. In addition to the data density being controlled by sedimentation rate, it also affects the variability of the palaeointensity (and subsequently the residuals after a fit). Given that each data point is itself an average of a time interval, the longer the time interval over which it averages, the less variable the data. This influences the values of our ML weights—which are derived from a pdf. Pdfs by definition, integrate to 1, such that if there is more variance in the data, the peak ends up being lower relatively speaking, which translates into the ML weights having a different average for each time-series. Therefore, we also normalize the weights by dividing by the average weight for each distribution. These normalization factors (N_k) are absorbed into the PML weights

$$N_k = \left(\frac{\Delta t}{n_k} \right) \left(\frac{1}{\frac{1}{n_k} \sum_{j=1}^{n_k} w_{k,j}} \right). \tag{B19}$$

B3 The combined problem: absolute and RPI series

For the joint inversion of API and several RPI data sets, we start with the assumption that each data set has a unique noise distribution [$f(\epsilon_i, \hat{\beta})$] and unique scale factor. For K data sets, this updates eqs (B12)–(B14) into

$$\frac{\partial l}{\partial \beta_j^q} = \sum_{k=1}^K \sum_{i=1}^{n_k} w_{k,i}^q c_j(t_{k,i}) \left[\tilde{d}_{k,i} - \sum_{j=1}^p \beta_j^q c_j(t_{k,i}) \right] = 0 \tag{B20}$$

$$w_{k,i}^q = N_k^{q-1} \left(\frac{\lambda \delta}{\sigma^{\lambda} \gamma^{\lambda}} \right)_k^{q-1} \left| \tilde{d}_{k,i} - \sum_{j=1}^p \beta_j^{q-1} c_j(t_{k,i}) \right|^{\lambda_k^{q-1} - 2} \tag{B21}$$

$$\tilde{d}_{k,i} = \zeta_k d_{k,i} - \mu_k^{q-1}. \tag{B22}$$

In matrix notation, in a scenario with $(K - 1)$ RPI records and one API data set

$$\begin{bmatrix} \mathbf{C}_1^T \\ \vdots \\ \mathbf{C}_{K-1}^T \\ \mathbf{C}_a^T \end{bmatrix} \begin{bmatrix} \mathbf{W}_1 & & & 0 \\ & \ddots & & \\ & & \mathbf{W}_{K-1} & \\ 0 & & & \mathbf{W}_a \end{bmatrix} \begin{bmatrix} \mathbf{C}_1 \\ \vdots \\ \mathbf{C}_{K-1} \\ \mathbf{C}_a \end{bmatrix} \hat{\beta} = \begin{bmatrix} \mathbf{C}_1^T \\ \vdots \\ \mathbf{C}_{K-1}^T \\ \mathbf{C}_a^T \end{bmatrix} \begin{bmatrix} \mathbf{W}_1 & & & 0 \\ & \ddots & & \\ & & \mathbf{W}_{K-1} & \\ 0 & & & \mathbf{W}_a \end{bmatrix} \begin{bmatrix} \zeta_1 \mathbf{S}_1 \\ \vdots \\ \zeta_{K-1} \mathbf{S}_{K-1} \\ \mathbf{A} \end{bmatrix}, \tag{B23}$$

where \mathbf{C} are cubic B-spline matrices, \mathbf{W} are weight matrices and \mathbf{A} and \mathbf{S} are data vectors of absolute and relative palaeointensities, respectively. $\hat{\beta}$ is the vector of model parameters: the coefficients for the B-splines.